

# Emplacement of laboratory igneous sheets and fingers influenced by the Mohr-Coulomb properties of the host

Frank Bo Buster Guldstrand<sup>1</sup>, Alban Souche<sup>2</sup>, Håvard Svanes Bertelsen<sup>2</sup>, Alain Zanella<sup>3</sup>, and Olivier Galland<sup>4</sup>

<sup>1</sup>The NJORD Center

<sup>2</sup>Physics of Geological Processes, The NJORD Center, Geosciences Department, University of Oslo, Norway

<sup>3</sup>Le Mans Université, Géosciences Le Mans, France

<sup>4</sup>The NJORD Center, Physics of Geological Processes

November 23, 2022

## Abstract

Planar magma intrusions such as dykes and sills are major magma transport features and the main feeders of volcanic eruptions. Among planar intrusions, sheet intrusions are fracture-like continuous conduits, which are assumed to form by tensile opening and dominantly elastic deformation of the host. However, numerous planar intrusions are not continuous, and consist of aligned finger-shaped or more lobate conduits. Field observations show that the emplacement of these fingers is associated with inelastic, shear failure of the host rock, suggesting that the Mohr-Coulomb properties of crustal rocks play a significant role in the emplacement of fingers. In this study, we test the effects of the Mohr-Coulomb properties of crustal rocks on the emplacement of sheet-shaped and finger-shaped intrusions through quantitative 2-dimensional laboratory experiments. The model magma is viscous Golden Syrup, and the model rock is made of mixtures of dry granular materials of variable cohesion. A sideview camera allows monitoring the shape of the propagating intrusions and the associated deformation in the host, and a pressure sensor monitors the pressure of the syrup. Our experiments show that sheet intrusions form in high-cohesion hosts whereas finger-shaped intrusions form in low-cohesion hosts. Deformation analysis of the host and pressure data show that the sheets and fingers result from drastically distinct dynamics: sheets dominantly propagate as a fracture, whereas fingers are emplaced as viscous indenters. All in all, our experiments highlight that the cohesion of the Earth's crust and the associated shear damage play a major role on planar intrusion emplacement.

1 **Emplacement of laboratory igneous sheets and fingers**  
2 **influenced by the Mohr-Coulomb properties of the host**

3

4 Frank Guldstrand<sup>1</sup>, Alban Souche<sup>1</sup>, Håvard Svanes Bertelsen<sup>1</sup>, Alain Zanella<sup>2</sup>, and Olivier  
5 Galland<sup>1\*</sup>

6 \*Corresponding Author: olivier.galland@geo.uio.no

7

8 <sup>1</sup>Physics of Geological Processes (PGP), The NJORD Centre, Dept of Geosciences UiO, Oslo,  
9 Norway,

10 <sup>2</sup>Le Mans Université, Géosciences Le Mans - LPG UMR 6112, 72085, Le Mans, France

11

12 **Keywords:** Magma Emplacement, Dyke, Sheet intrusion, Finger intrusion, Host  
13 Rock Deformation, 2D Laboratory Model

14

---

15 **Abstract**

16 Planar magma intrusions such as dykes and sills are major magma transport features  
17 and the main feeders of volcanic eruptions. Among planar intrusions, sheet intrusions  
18 are fracture-like continuous conduits, which are assumed to form by tensile opening  
19 and dominantly elastic deformation of the host. However, numerous planar intrusions  
20 are not continuous, and consist of aligned finger-shaped or more lobate conduits. Field  
21 observations show that the emplacement of these fingers is associated with inelastic,  
22 shear failure of the host rock, suggesting that the Mohr-Coulomb properties of crustal  
23 rocks play a significant role in the emplacement of fingers. In this study, we test the  
24 effects of the Mohr-Coulomb properties of crustal rocks on the emplacement of sheet-  
25 shaped and finger-shaped intrusions through quantitative 2-dimensional laboratory  
26 experiments. The model magma is viscous Golden Syrup, and the model rock is made  
27 of mixtures of dry granular materials of variable cohesion. A sideview camera allows  
28 monitoring the shape of the propagating intrusions and the associated deformation in  
29 the host, and a pressure sensor monitors the pressure of the syrup. Our experiments  
30 show that sheet intrusions form in high-cohesion hosts whereas finger-shaped  
31 intrusions form in low-cohesion hosts. Deformation analysis of the host and pressure  
32 data show that the sheets and fingers result from drastically distinct dynamics: sheets  
33 dominantly propagate as a fracture, whereas fingers are emplaced as viscous indenters.

34 All in all, our experiments highlight that the cohesion of the Earth's crust and the  
35 associated shear damage play a major role on planar intrusion emplacement.

---

36

37

## 38 **Introduction**

39 The emplacement of dykes and sills in the Earth's crust is a fundamental process in the  
40 transport of magma and feeding volcanic eruptions [*Halls and Fahrig, 1987; Rivalta et*  
41 *al., 2015; Tibaldi, 2015; Magee et al., 2016; Galland et al., 2018*]. Understanding the  
42 emplacement mechanics of magmatic intrusions allows for an improved understanding  
43 of the Earth system, but it is also of applied importance in terms of hazard mitigation  
44 and natural resource exploration [*Senger et al., 2017; Guldstrand et al., 2018; Rabbel*  
45 *et al., 2018*]. Dykes and sills usually overall exhibit long and thin planar shapes, i.e.,  
46 igneous sheets, similar to those of fractures. Based on this resemblance, most dyke and  
47 sill emplacement models have assumed that they form as tensile fractures propagating  
48 through elastic medium [e.g. *Pollard, 1987; Bungler and Cruden, 2011; Galland and*  
49 *Scheibert, 2013; Rivalta et al., 2015*]. According to this mechanism, dykes and sills are  
50 expected to be continuous and to exhibit sharp tips accommodating tensile opening of  
51 the host rock, as supported by field observations [Figure 1; *Galland et al., 2018; Poppe*  
52 *et al., 2020*].

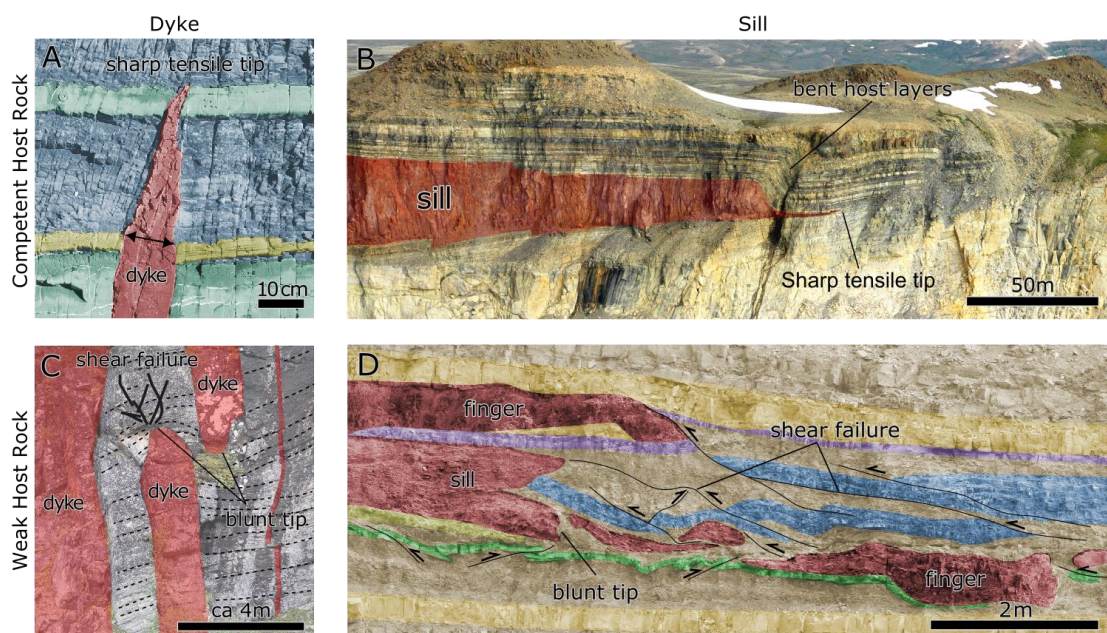
53 All planar intrusions emplaced in the brittle crust, however, do not exhibit  
54 shapes and structures that are compatible with the sheet intrusion emplacement  
55 mechanism. For example, numerous igneous sills exhibit lobate morphologies, so-  
56 called finger shapes [*Pollard et al., 1975; Schofield et al., 2012; Galland et al., 2019*].  
57 Detailed field observations and 3D seismic data analysis of fingers show that even if  
58 the overall apparent shapes of these intrusions look like sheets, they are discontinuous  
59 and the tips of individual segments are blunt, i.e. everything but sharp [*Pollard et al.,*  
60 *1975; Schofield et al., 2012; Spacapan et al., 2017; Galland et al., 2019; Kjøl et al.,*  
61 *2019*]. In addition, the visible structures accommodating the propagation of the fingers'  
62 tips dominantly exhibit shear, compressional failure of the host rock [*Pollard et al.,*  
63 *1975; Duffield et al., 1986; Spacapan et al., 2017; Galland et al., 2019*].

64 The structural differences between sheet- and finger-shaped intrusions resides  
65 principally in contrasting mechanical behaviors of their host rock, especially on their  
66 failure modes (tensile versus shear). Tensile and shear failure modes are fundamental

67 features of the Mohr-Coulomb-Griffith failure criteria of brittle rocks, and their  
 68 occurrence depends on parameters such as rock cohesion and angle of friction [Fig. 1;  
 69 *Jaeger et al., 2009; Abdelmalak et al., 2016*]. The different failure modes associated  
 70 with sheet and finger intrusions leads to the main working hypothesis this paper intends  
 71 to test: Mohr-Coulomb properties of crustal rocks, and in particular their cohesion,  
 72 control the emplacement of igneous sheets versus igneous fingers.

73 We propose to test this hypothesis through quantitative quasi-2D laboratory  
 74 models of model magma intrusion with strong (high cohesion) to weak (low cohesion)  
 75 model host rocks. The model magma used was viscous golden syrup injected at a  
 76 constant flow rate at room temperature with pressure monitored at the inlet. In order to  
 77 decipher between distinctive deformation modes accommodating the emplacement of  
 78 the syrup, the model rock displacements were monitored using a Digital Image  
 79 Correlation (DIC) algorithm available through the open source photogrammetric  
 80 structure-from-motion software MicMac [*Galland et al., 2016*]. Our results show that  
 81 cohesion has a significant control on the emplacement mechanics on the intrusion of a  
 82 viscous fluid. Higher cohesion hosts result in sheet emplacement while lower cohesion  
 83 hosts result in the emplacement of finger intrusions with drastically different  
 84 emplacement mechanics at work evident in deformation and pressure monitoring.

85  
 86



87  
 88

89 **Figure 1.** A,B sharp tipped tensile sheet intrusions into competent host rock. C,D Blunt tipped intrusions  
90 associated with shear failure into weak host rock [*Spacapan et al.*, 2017; *Galland et al.*, 2018; *Kjøll et*  
91 *al.*, 2019; *Poppe et al.*, 2020].

92

93

94

## 95 **Method**

### 96 *Experimental setup*

97 The experimental setup is an improved version of that of *Abdelmalak et al.* [2012]. It  
98 consists of a 30 mm thick 2D Hele-Shaw cell with dimensions 80 cm wide and 50 cm  
99 high (Fig. 2). The frame consists in total of 4 separate aluminum bar profiles. Front and  
100 back glass panes are kept in place with clamps and gaskets. The inlet consists of a  
101 rectangular 1 mm wide, 3 cm high, slit in order to promote the initiation of a vertical  
102 sheet intrusion; it is an interchangeable separate piece attached to the center of the two  
103 bottom aluminum profiles. Rubber gaskets ensure a tight seal of the inlet to the glass.  
104 A simple tube system connects a syringe-pump to a pressure sensor before proceeding  
105 to the inlet. The syringe pump injects the model magma at constant volumetric flow  
106 rate.

107

### 108 *Materials*

109 The model host rock consists of 4 different mixes of silica flour and glass microbeads  
110 (table 1). These two fine-grained materials fail according to a Mohr-Coulomb criterion  
111 [*Abdelmalak et al.*, 2016]. The glass bead flour (GB) has a modal grain size of 30  $\mu\text{m}$   
112 and is nearly cohesionless as it collapses under its own weight. Silica flour (SF) has a  
113 modal grain size of 10-20  $\mu\text{m}$  and is cohesive when compacted. As such, SF does not  
114 collapse under its own weight and sustains vertical walls [*Galland et al.*, 2006].  
115 *Abdelmalak et al.* [2016] showed that the cohesion of GB/SF mixes follows a near linear  
116 trend with respect to mixing proportion, so that these mixes allow us to explore the  
117 effect of variable cohesion on the modeled processes. We added 7wt% of black  
118 aluminum silicate powder, with a grain size of 0.2-0.6 mm, to the flour mixes to add  
119 texture to the host. This was in order to apply Digital Image Correlation (DIC) to track  
120 the deformation induced by the propagating model magma. We tested that the addition  
121 of the tracer did not significantly affect the cohesion of the mix.

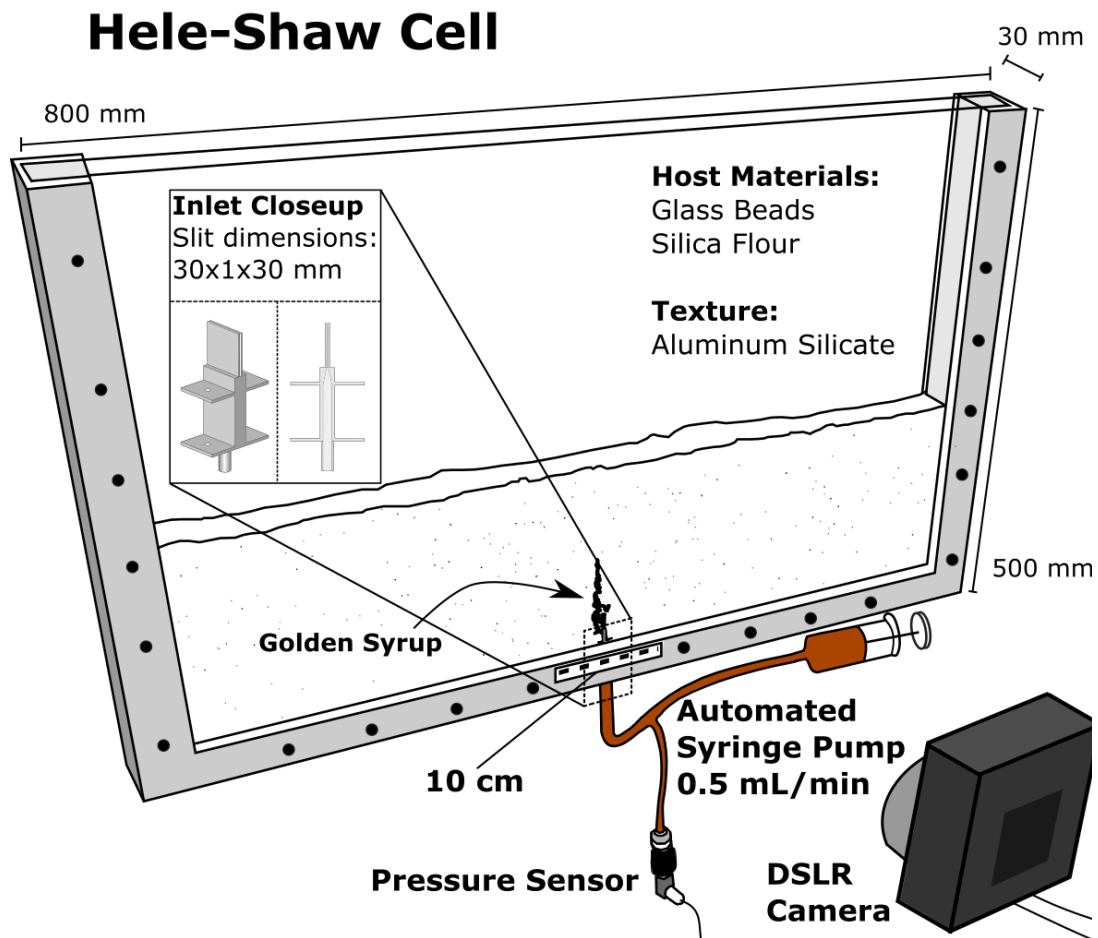


**Figure 2** Dimensions of Hele-Shaw cell including a compacted mix of cohesive silica flour and glass beads into which golden syrup is injected through the use of an automated syringe pump at 0.5 ml/min. Monitoring is done through recording of pressure and a camera taking photographs each 120/180 s depending on the mix used. We then apply digital image correlation (DIC) to the series of processed images.

123

124 The model magma, Lale & Tate's Golden Syrup, is a commonly used fluid in intrusion  
 125 experiments [e.g. *Mart and Dauteuil, 2000; Mathieu et al., 2008; Delcamp et al., 2012*].  
 126 The injection was done at room temperature ( $\sim 21^\circ\text{C}$ ), at which we measured the  
 127 viscosity ( $\sim 55 \text{ Pa s}$ ) and the density ( $\sim 1440 \text{ kg m}^{-3}$ ) of the syrup. This is in agreement  
 128 with reported values of *Llewelin et al. [2002]* and *Beckett et al. [2011]*. The wettability  
 129 of the golden syrup was tested in combination with the silica flour, glass beads and  
 130 glass by measuring the contact angle in air using the DSA drop shape analyzer from  
 131 Krüss. From this we concluded that Golden Syrup was non-wetting in all cases for the  
 132 time scale of an experiment. The non-wetting property and the small grain size ensure

133 fluid propagation occurred mainly through fracturing and pushing the host material,  
134 and not through percolation and porous flow.

135           The suitability of the model materials to simulate viscous magma  
136 emplacement in the brittle crust has been discussed in detail by [Abdelmalak *et al.*,  
137 2012]. Given the size of our laboratory setup and the range of cohesion of the model  
138 crust, 1 cm in our experiment scales to 10-100 m in nature. In that scale, the high-  
139 cohesion materials simulate competent rocks (i.e. limestone, consolidated sandstone,  
140 plutonic rocks, etc.) whereas the low cohesion materials simulate weak rocks (i.e. shale,  
141 poorly consolidated sandstone, volcanic tuff, etc.) [Abdelmalak *et al.*, 2016].

142

### 143 *Experiment Protocol*

144 To prepare an experiment, first the inlet is plugged, and a known mass of flour is poured  
145 into the cell. The flour mix must not be poured into the cell too carefully as it will  
146 enhance sorting of the aluminum silicate grains, and so decrease the quality of the  
147 texture that is necessary for DIC. A heavy metal bar with a handle is placed on top of  
148 the flour within the cell; a water level is used to ensure that a flat and level surface is  
149 achieved. We then compact the flour using a high- frequency shaker running on  
150 compressed air (Houston Vibrator, model GT-25). The heavy metal bar was lined with  
151 a porous foam so that when lifted it did not create suction and disturbance of the  
152 compacted flour. This procedure ensures a homogeneous and repeatable compaction.

153

154 **Table 1.** Experiment parameters and model host rock properties

Exp Nr	$V_{inj}$ (mL min <sup>-1</sup> )	Mix (GB/SF)	Mass (kg)	Depth (cm)	Density (kg m <sup>-3</sup> )	Compaction % <sup>a</sup>	Cohesion (Pa) <sup>b</sup>	Temp (C)	Erupt Time (Min)
16	0,5	90/10	7,5	16,2	1652,8	2,5	239.5	21,1	52
24	0,5	90/10	7,5	16,75	1606,7	6,0	239.5	21	77
14	0,5	80/20	7,5	16,2	1652,8	4,0	313.1	21,3	54
23	0,5	80/20	7,5	15,9	1679	10,4	313.1	20,9	48
19	0,5	50/50	6,5	16,3	1425	14,6	374.96	20,6	69
20	0,5	50/50	6,5	16,8	1388,9	13,9	374.96	21,6	82
21	0,5	0/100	4,5	14,2	1107,1	14,4	559.91	21	96
22	0,5	0/100	4,5	15,1	1052	14,6	559.91	21,5	130

155 <sup>a</sup>Compaction between measured and initial density and final compacted density.156 <sup>b</sup>From *Abdelmalak et al.* [2016].

157

158 The amount of compaction differs between the mixes, as pure GB does not compact  
 159 much, whereas pure SF compacts up to ~15%. For each mix, we compacted the  
 160 maximum amount, a range of 3-15% compaction, resulting in final densities of 1052-  
 161 1652.8 kg m<sup>-3</sup> (0/100 GB/SF and 90/10 GB/SF respectively). The inlet plug was  
 162 removed after compaction.

163 The viscous golden syrup was put into a syringe and allowed to degas during  
 164 the model host rock preparation. The syringe was then put into the syringe pump and  
 165 connected to the inlet. A pressure sensor was connected to the injection system with a  
 166 T-connector in-between the pump and inlet. All experiments were performed with a  
 167 constant flow rate of 0.5 ml min<sup>-1</sup> resulting in experiment durations of ~52- 130 min.  
 168 The pressure data has been smoothed using a Savitsky-Golay filter applied equally to  
 169 all pressure data to remove oscillations inherent to the syringe pump and tube system.  
 170 However due to the low injection velocity and the high viscosity of the fluid we deem  
 171 that the effects of such oscillations are negligible.

172 A DSLR camera (NIKON D3200) took pictures of one side of the  
 173 experiment (Fig. 2) at constant framing rate to monitor the evolution of the model  
 174 dykes. The camera and pump triggers, as well as the pressure logging, were integrated  
 175 and synchronized via a custom designed Arduino system.

176

177 *Deformation Monitoring*

178 The side view photographs are used to compute maps of displacements induced by the  
179 intruding syrup within the model crust. We corrected the optical distortion of the lens  
180 by taking a series of pictures of a checkerboard, of known size, attached to the front  
181 glass plate of the cell after each experiment. The image distortion correction was  
182 calculated using the image toolbox available in MATLAB. The image toolbox also  
183 allows for adaptively adjusting the contrast of the image, enhancing the texture. We  
184 then applied DIC using the MM2DPosSism-algorithm, which has been specifically  
185 designed to detect very small displacements [Galland *et al.*, 2016]. This algorithm is  
186 available through the free open-source structure-from-motion software MicMac  
187 developed by the French National Geographic Institute IGN [Rosu *et al.*, 2015; Rupnik  
188 *et al.*, 2017]. This allows us to compute displacements smaller than 0.1 mm between  
189 images [e.g. Galland *et al.*, 2016]. The MM2DPosSism-algorithm is most successful  
190 for a given range of displacements. In order to give the best displacement results, we  
191 adjusted the temporal resolutions in our experiments. For the experiments in 90/10 and  
192 80/20 mixes, which were shorter in duration, the temporal resolution was 120 s. The  
193 experiments in 50/50 and 0/100 mixes, which were longer in duration and of smaller  
194 displacements, the temporal resolution was 180 s.

195

## 196 **Results**

### 197 *Intrusion Characteristics*

198 We produced experiments using 4 different mixes of cohesive Mohr-Coulomb host  
199 material. Each experiment was performed twice to test the repeatability of our results.  
200 These repeated experiments exhibited consistent results with the first experiment using  
201 the same cohesion. The repeatability of this type of experiment has also been  
202 thoroughly demonstrated by *Abdelmalak et al.* [2012]. All experiments used an inlet  
203 depth of ~16 cm, except the 100% SF experiments (0/100) where the inlet depths were  
204 14.2 and 15.1. Shallower depths were chosen as attempts at 16 cm depth failed to  
205 produce eruptions because the intrusions were significantly thicker than those in the  
206 other experiments, such that the available syrup volume in the pump was insufficient.

207 A typical experiment started with chaotic emplacement of the syrup,  
208 resulting in complex branching nucleating from the inlet. However, the dominant  
209 vertical flow from the inlet ultimately forced a sub-vertical intrusion to form,  
210 propagating in a relatively stable fashion. At a certain depth, the intrusion changed

211 behavior. Its tip either deviated from vertical (Fig. 3) or bifurcated into two small  
212 branches (Fig. 3). In the following sections, we will refer to this transition depth as the  
213 *critical depth*. Subsequently, the syrup keeps ascending until erupting at the surface.  
214 All of the intrusions were associated with uplift and surficial extensional fractures  
215 parallel to the intrusion and perpendicular to the cell. Some extensional fractures can  
216 close and migrate as the intrusion approached the surface. The intrusion could also  
217 cause the basal uplift of a block of the host. These observations are consistent with  
218 those of *Abdelmalak et al.* [2012]. Although this general description fits all our  
219 experiments the differences which will be detailed in the following paragraphs.

220           In the high cohesion hosts (50/50 and 0/100 mixes, Fig. 3C, D), the  
221 intrusions were planar in geometry, perpendicular to the glass walls, clearly splitting  
222 the flour in two blocks. The initial chaotic branching near the inlet was less than in the  
223 low cohesion experiments; note, however, that the bottom branches grew during the  
224 duration of the experiments. The stable ascending intrusions exhibit a clear sheet shape,  
225 until it reached the critical depth. In the 50/50 mix experiment, the intrusion grew  
226 continuously and inclined after reaching the critical depth (Fig. 3C). Conversely, in the  
227 0/100 mix experiment (the highest cohesion), the intrusion tip arrested at the critical  
228 depth, resulting in thickening of the sheet, until the overburden failed (Fig. 3D). At the  
229 critical depth, the intrusion tip split in two small branches (Fig. 3D middle column),  
230 and subsequently one branch took over to accommodate for the syrup propagation (Fig.  
231 3D right column). In these experiments, significant uplift can only be seen after the  
232 intrusion crossed the critical depth.

233           For lower cohesion hosts (90/10 and 80/20 mixes, Fig. 3A, B), the intrusions  
234 exhibited a more undulating and branching geometry. In the experiment with the 90/10  
235 mix, the intrusion did not appear as a perfect continuous sheet, so that it did not split  
236 the entire host in two (Fig. 3A). Instead, the intrusion exhibited a finger structure, such  
237 that blocks of the host material remained between the intrusion and glass walls. As a  
238 result, the intrusion appeared as disconnected segment along the photographed glass  
239 plate, while they were connected in the third dimension. In the experiment with the  
240 80/20 mix, the base of the intrusion was thick enough to constitute planar sheet  
241 geometry (Fig. 3B). Significant uplift was visible already when the intrusion was at  
242 depth, i.e. under the critical depth. At the critical depth, a hybrid form of damage ahead  
243 of the intrusion was observed, i.e. distributed damage throughout the wedge of material

244 above the intrusion and small extensional open fractures at the surface. These fractures  
245 were more prominent in the 80/20 mix host than in the 90/10 mix host (Fig. 3A, B).  
246

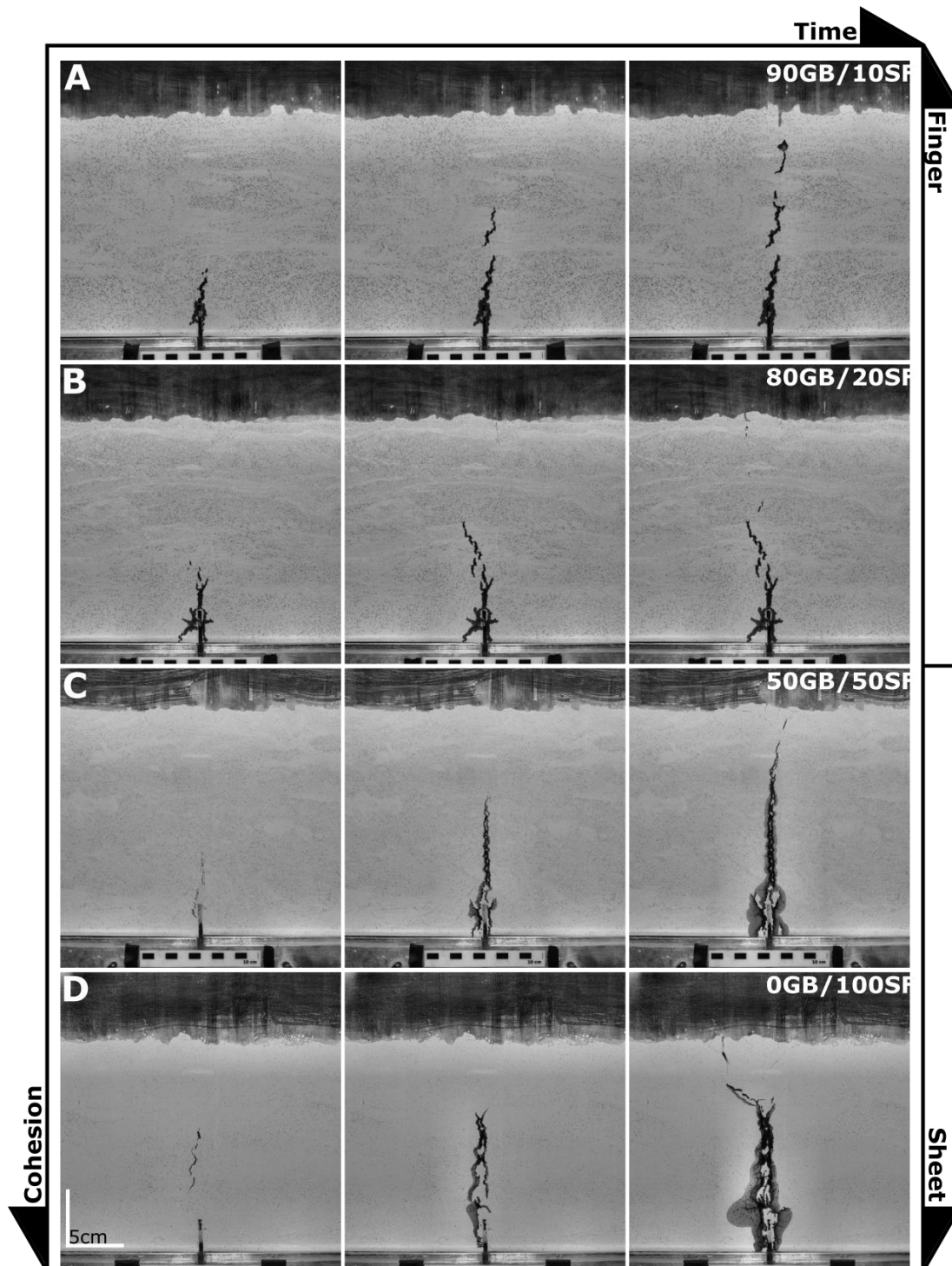


**Figure 3.** The rows show intrusion into a compacted mix of 90 wt% glass beads and 10% silica flour (A), 80/20 (B), 50/50 (C) and 0/100 (D). Columns show experiment photos at an initial, intermediate and late time step. The time steps were chosen such that they show intrusion initiation, a period of stable vertical propagation and the critical depth where failure of the overburden occurs. Experiments

in 50/50 (C) and 0/100 (D) comprise sheet intrusions while only the base of the 80/20 (B) intrusions are of sheet geometry. Accelerated experiment videos are available in supplemental material S1.

247

### 248 *Propagation Velocity*

249 The experiment durations differed, even if the injection rate was constant. The  
250 experiment duration was in general shorter for low cohesion experiments and longer  
251 for high cohesion experiments, implying distinct propagation velocities. We measured  
252 the propagation velocity of the intrusion tips using simple image analysis (Fig. 4; left  
253 column). The highest point of the intrusion was then extracted at each time step.  
254 However, in the initial and final time steps, because of the complex shapes of the  
255 intrusions, we may not adequately track the propagating tips. In addition, during the  
256 initial timesteps, the intrusion is often not yet observable. Thus, for the time steps earlier  
257 than the first visible occurrence of the liquid on the photographs, we set a constant value  
258 corresponding to the depth of the intrusion tip at its first documented position. Thus,  
259 the analysis presented in Fig. 4 (left column) is most relevant in the stable phase of  
260 propagation of the intrusion, i.e. the intermediate part. We interpolated the discrete  
261 measurements of the depth of the intrusion tips to a continuous curve (Fig. 4; red line  
262 in left column), allowing us to compute propagation velocity of the intrusion tips (Fig  
263 4; right column).

264

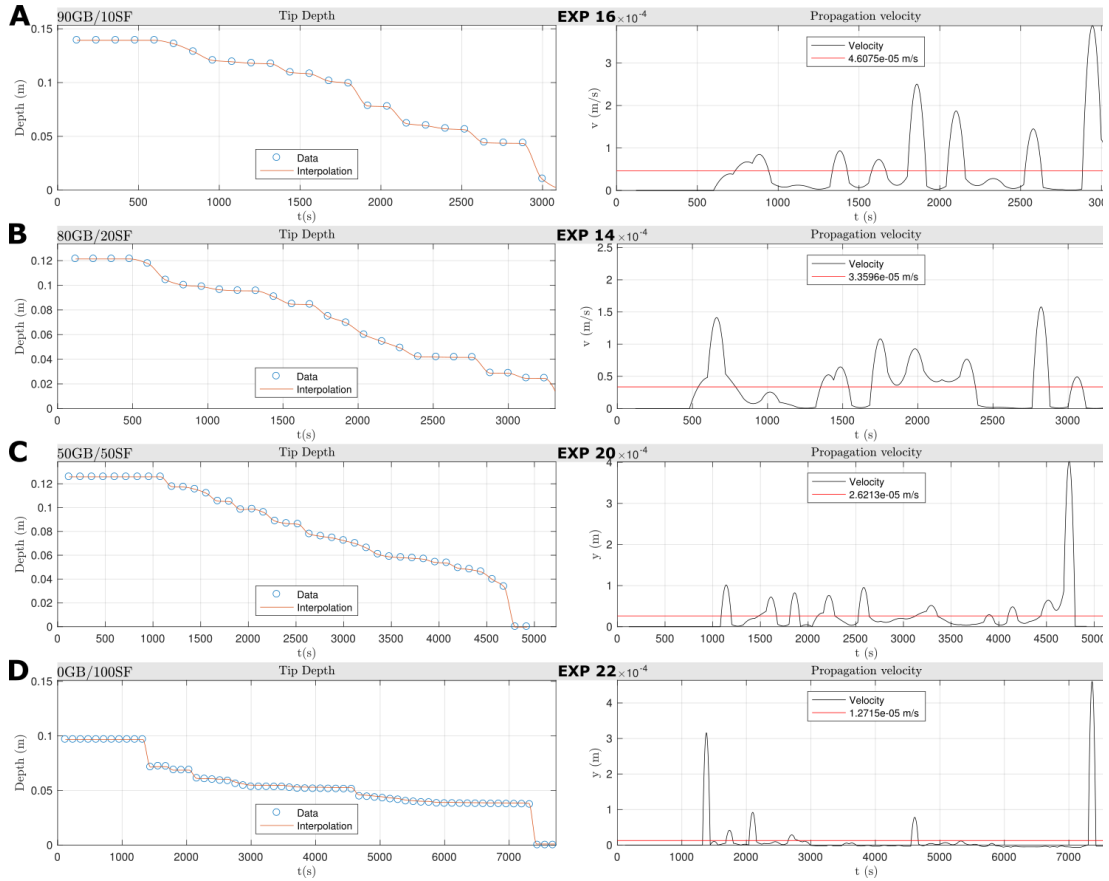


**Figure 4.** Left plots in each row show the depth of the intrusion tip identified in the experiment pictures using an interval of 120 s. The right plots show the vertical propagation velocity calculated from the intrusion depth and time. The average propagation velocity is plotted in red and presented in the legend. During initial time steps we cannot track the intrusion tip until the intrusion is visible therefore the initial values are set to the constant depth where the intrusion is first visible. During final time steps due to the damage created ahead of the intrusion and the creation of open fractures it also makes the intrusion difficult to track. Plots of additional experiments are available in the supplemental material S2.

265

266

267

268 The average propagation velocity (red horizontal line in right column of  
 269 Fig. 4) decreases from  $\sim 0.5 \times 10^{-5} \text{ m s}^{-1}$  to  $\sim 0.15 \times 10^{-5} \text{ m s}^{-1}$  with increasing cohesion of  
 270 the host material. We note as well that the propagation was not steady, with periods of  
 271 slow, even no, propagation alternating with sudden accelerations, i.e. burst-like  
 272 behavior. There are many more bursts in the low cohesion experiments than in the high  
 273 cohesion ones.

273

274 *Horizontal Displacements*

275 Figure 5 displays time series of maps of horizontal displacements  $U_x$ . In all  
276 experiments, the displacements are rightward to the right of the intrusions and leftward  
277 to the left of the intrusions, indicating opening of the host to accommodate the  
278 emplacement of the intrusions. The maximum displacement values are along the walls  
279 of the intrusions, and the displacements decrease gradually away from the intrusions,  
280 marking displacement halos on each side of the intrusions.

281           However, we can notice differences between the low and high cohesion  
282 experiment. In the high cohesion experiments (50/50 and 100/0), the  $U_x$  opening occurs  
283 along the entire length of the growing intrusions (Fig. 5C, D). Little or no horizontal  
284 displacement is detected in the overburden when the intrusion is below the critical  
285 depth. When the intrusion reaches the critical depth, the displacement along the deeper  
286 part of the intrusion walls decreases or ceases. From this time on, displacements mainly  
287 affect the shallower part of the host, in between the critical depth and the surface (Fig.  
288 5C, D).

289           The  $U_x$  displacements in the low cohesion experiments (90/10 and 80/20),  
290 before the intrusion reaches the critical depth, concentrate in the very upper parts of the  
291 intrusions, and even extend shallower than the intrusion tips (Fig. 5A, B). Conversely,  
292 the bottom parts of the intrusions exhibit no horizontal displacement at all. After the  
293 intrusion reaches the critical depth, it triggers horizontal displacements that extended  
294 until the model surface. We note that in the early stage of the 80/20 experiment, the  
295 initial sheet triggered horizontal displacement that extended along the entire intrusion  
296 (Fig. 5B). The displacement subsequently localized close to the intrusion tip.

297           Videos of all horizontal displacements are available in the supplemental  
298 material S2.

299

300

301

302

303

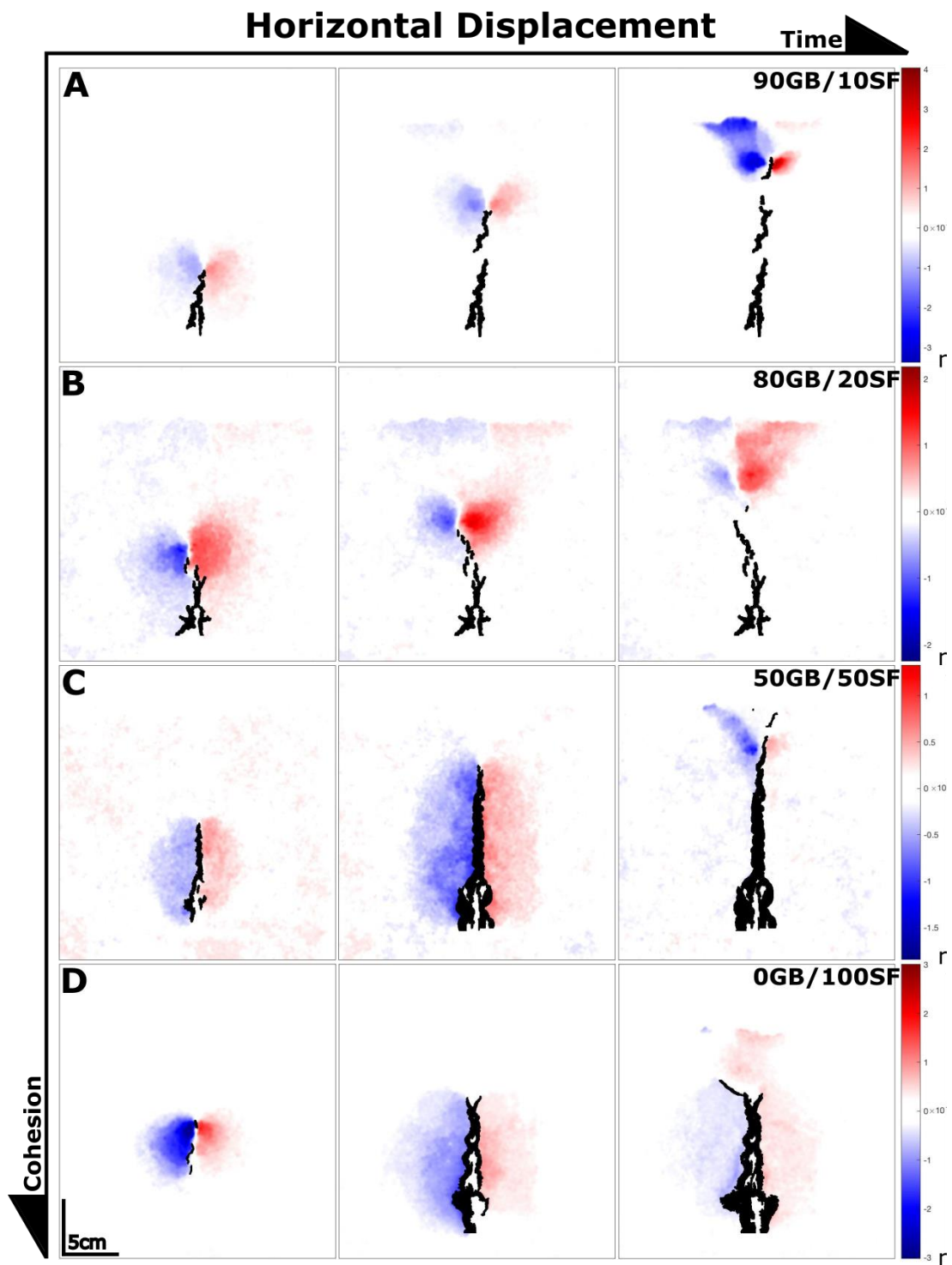


**Figure 5.** The rows show intrusions (black) into mixes of 90/10 (A), 80/20 (B), 50/50 (C) and 0/100 (D). Columns show experiment photos at an initial, intermediate and late time step. A and B shows that deformation, during propagation, is mainly concentrated to and beyond the intrusion tip. C and D show the entire fracture being active and displacing during vertical propagation. Once the critical depth is reached, the overburden fails and pathways were created for the fluid to utilize for the final ascent and any opening of the intrusion ceased. Accelerated experiment videos are available in supplemental material S1.

304

### 305 *Vertical Displacements*

306 Figure 6 displays time series maps of vertical displacement  $U_y$ . Overall, the intrusions  
307 triggered uplift only, mostly restricted in the overburden of the intrusions. In the  
308 weakest host (90/10), widespread uplift occurred above the intrusion tip already at a  
309 very early deep stage of intrusion emplacement. This uplift affected the entire  
310 overburden, from the tip of the intrusion up to the surface (Fig. 6A). The uplift  
311 magnitude increases as propagation occurs, but remains constrained above the intrusion  
312 tip. This implies that the uplifted domain reduced in size during the propagation of the  
313 intrusions. The boundaries of the uplifting domain were gradual. Once the critical depth  
314 is reached and the overburden fails, the majority of the displacements cease with the  
315 exception of minor displacements of blocks as the fluid propagates to the surface. A  
316 similar evolution is observed in the 80/20 experiment (Fig. 6B). However, the  
317 deformation field displays discontinuities that suggest the occurrence of faults that  
318 partly dissect the uplifted domain.

319           In the more cohesive 50/50 experiments, the early and intermediate  
320 propagation of the intrusions did not trigger significant uplift of their overburden,  
321 except small sporadic patches (Fig. 6C). However, as the intrusion tip approaches the  
322 critical depth, sudden substantial uplift affected the overburden (Fig. 6C). We notice  
323 that the center of the uplifted domain is off-centered to the left with respect to the  
324 underlying intrusion in both 50/50 experiments; in these experiments, the intrusion  
325 deviated rightward after crossing the critical depth. The 0/100 experiment displayed  
326 more prominent patches of uplift at depth until the overburden reached its critical depth  
327 (Fig. 6D). At this point there is widespread uplift dominantly above the intrusion. The  
328 repeated experiment clearly shows asymmetric uplift with one side of the host being  
329 uplifted (Supplemental material S2).

330           Videos of all vertical displacements are available in the supplemental  
331 material S2.

332



333

### 334 *Shear Strain*

335 The horizontal and vertical displacement maps in the host material allow for calculating  
336 time series maps of shear strain,  $\gamma = \frac{1}{2} \left( \frac{\partial U_x}{\partial y} + \frac{\partial U_y}{\partial x} \right)$ , as the intrusion propagates (Fig. 7).  
337 As the displacements are small, this analysis is prone to noise so smoothing has been  
338 applied to the data before calculating the shear strain. Videos of the shear strain in all  
339 the experiments are available in the supplemental material S2.

340 The experiment with the 90/10 host, i.e. low cohesion, show prominent  
341 bands of reverse shear strain rooted on the intrusion tip. Already at depth, there are two  
342 inclined bands extending out from the intrusion tip (Fig. 7A; left column). These shear  
343 bands are persistent while the intrusion propagates upwards until the critical depth,  
344 where the shear bands curve and extend from the intrusion tip to the surface, signaling  
345 failure of the overburden. The shear bands display similar characteristics in the 80/20  
346 mix but appear slightly larger in extent (Fig. 7B).

347 In the experiments with higher cohesion hosts (Fig. 7C, D), shear strain is  
348 generally smaller in magnitude and restricted to smaller domains. Small, inclined  
349 reverse shear bands extend beyond the visible intrusion tip already at depth and during  
350 propagation. However, these are visible only intermittently and are shorter than in the  
351 lower cohesion experiments. Sporadically, the shear bands appeared asymmetrically,  
352 i.e. only the left or right shear band was visible. During propagation at depth, small  
353 shear strains intermittently occurred below the intrusion tip, i.e. along the walls of the  
354 dyke (Fig. 7C, D). Once the intrusion reached the critical depth, failure of the  
355 overburden initiated and bands of localized shear strain emanated from the tip to the  
356 intrusion to the surface (Fig. 7C, D). At this point in time, shear strains concentrate only  
357 in the overburden of the intrusions and the small shear strains below the intrusion tip  
358 ceased. We note as well that in the high cohesion experiment (0/100), shear bands  
359 gradually developed at the critical depth as the intrusion arrested and subsequently  
360 forms a split tip (Fig. 7D). One of the arms grows larger and later serves as the main  
361 conduit for the eruption while the other ceased to be active (Fig. 7D; right column).

362 In all experiments, when the intrusion reaches its critical depth, the observed  
363 localized shear bands affecting the overburden generally curve from the intrusion tip to

364 the surface, steepening as they came shallower, and finally intersecting with the surface  
 365 almost perpendicularly.  
 366

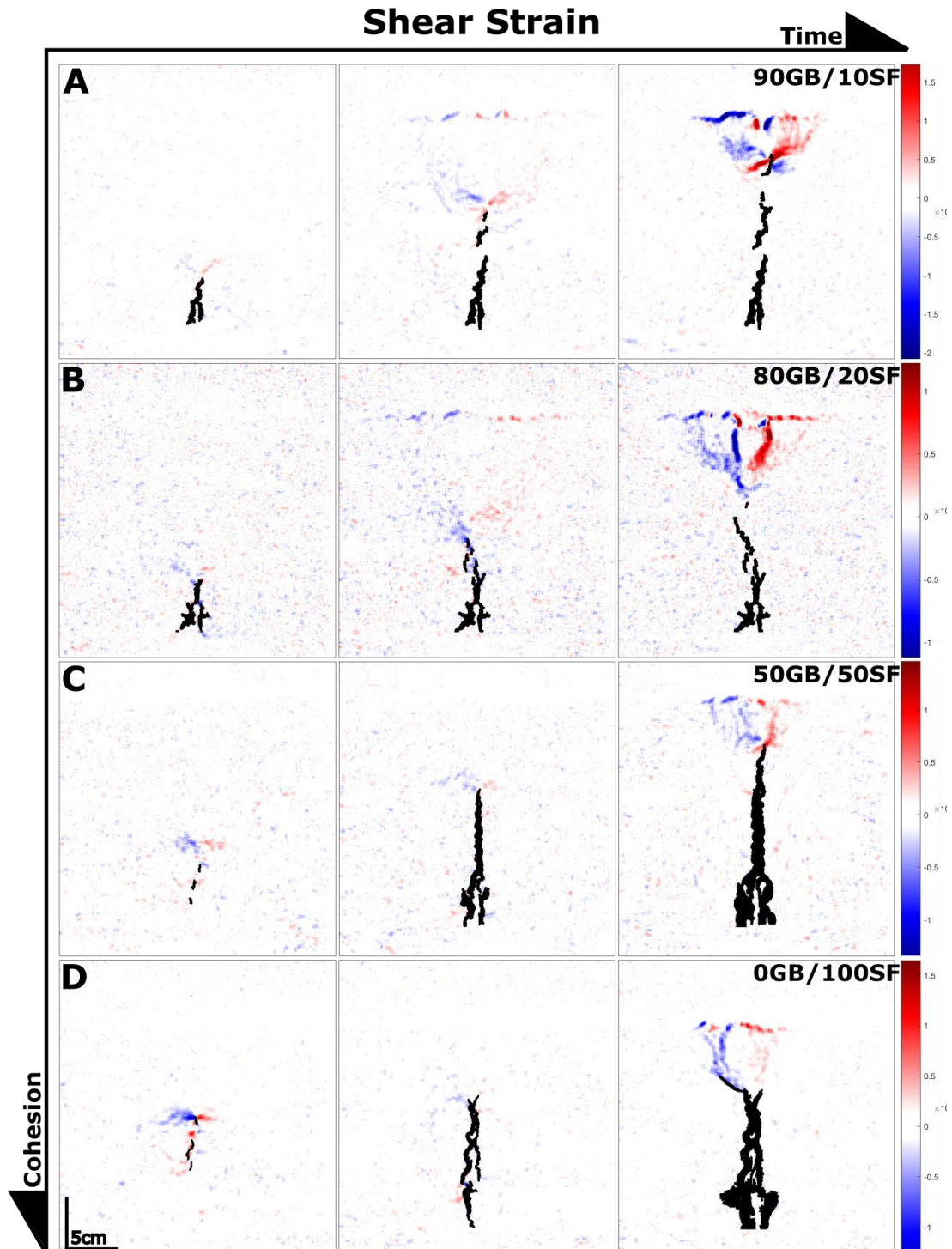


**Figure 7.** The rows show intrusions (black) into mixes of 90/10 (A), 80/20 (B), 50/50 (C) and 0/100 (D). Columns show experiment photos at an initial, intermediate and late time step. The computed shear strain in A and B extends from the intrusion already at depth until ultimately causing critical failure of the overburden. C & D shows smaller zones of shear associated with the intrusion tip. The

scale has been limited enhance smaller shear strains at depth. Accelerated experiment videos are available in supplemental material S2.

367

### 368 *Pressure and Displacement Analysis*

369 The pressure evolution curves for the low cohesion and high cohesion experiments  
370 show drastically distinct behaviors. In the low lower cohesion experiments, an initial  
371 pressure buildup is followed by a gradual pressure decrease until eruption occurs (Fig.  
372 8A, B). In contrast, in the higher cohesion experiments (Fig. 8C, D), an initial rapid  
373 pressure build-up is followed by a rapid pressure drop. After this initial pressure peak,  
374 pressure gradually increases until a second pressure drop occurs just before eruption.

375

376 In one of the 80/20 host experiments, a very small pressure drop occurred after the  
377 initial pressure build-up, while the early stage intrusion displayed sheet intrusion  
378 properties, similar to the high cohesion experiments. One of the 90/10 host experiments  
379 also displayed a late-stage pressure drop prior to eruption (available in supplemental  
380 material S2).

381 The initial pressure peak appears to anticorrelate with cohesion, as initial  
382 pressure peak in the lower cohesion experiments are higher ( $3-4 \times 10^4$  Pa) than in the  
383 higher cohesion experiments ( $1.5-2.5 \times 10^4$  Pa; Fig. 8). Admittedly, the lower cohesion  
384 hosts exert a higher lithostatic stress but even when accounting for this difference the  
385 pressure and cohesion anticorrelation remains. In all experiments, the pressure after  
386 eruption ranges between  $0.9 - 1.5 \times 10^4$  Pa with the low cohesion host experiments  
387 being at the higher end of this range.

388 To interpret the pressure evolution curves in terms of intrusion dynamics,  
389 we attempt to correlate the evolution of pressure with the deformational evolution of  
390 the host. To do so, we filter the horizontal and vertical displacement maps from noise  
391 and compute the average incremental displacements throughout the experiment:  $U_{xR}$   
392 for horizontal displacements to the right,  $U_{xL}$  for horizontal displacements to the left  
393 and  $U_y$  for vertical displacements. This calculation provides a combined measure of the  
394 magnitude of displacement and of the displaced area (Fig. 8). In the lowest cohesion  
395 experiment (Fig. 8A), the average horizontal displacements  $U_{xR}$  and  $U_{xL}$  initiate once  
396 the initial pressure peak has been reached. Then  $U_{xR}$  and  $U_{xL}$  reach a plateau between  
397  $\sim 750$  s, when stable vertical propagation initiates, and  $\sim 2500$  s when the intrusion

398 reaches the critical depth and failure of the overburden occurs. The average vertical  
399 displacement  $U_y$  also initiates at an early stage ( $\sim 500$  s), and gradually increases until  
400 reaching a constant value at  $\sim 2000$  s. This increasing stage corresponds to the uplift of  
401 a triangular area of the intrusion overburden that transitions into a stable stage due to  
402 the narrowing of the uplifting cone counterbalanced by the increased uplift magnitude  
403 (Fig. 6A; left and right column).

404 In the 80/20 host (Fig. 8B),  $U_{xR}$  and  $U_{xL}$  gradually increase between  $\sim 300$  s  
405 and  $\sim 1500$  s, while the sheet intrusion lengthens; subsequently,  $U_{xR}$  and  $U_{xL}$  reach a  
406 short plateau before decreasing in value from  $\sim 2300$  s, before eruption. The evolution  
407 of  $U_y$  displays a similar trend to the experiment using a 90/10 mix. The main difference  
408 being that  $U_y$  does not reach a plateau and instead suddenly decreases after reaching its  
409 maximum value at  $\sim 2300$  s (Fig. 8A). We attribute this shortened plateau to the  
410 increased cohesion of the host allowing localized failure to occur and create pathways  
411 ahead of the intrusion.

412 In both experiments with higher cohesion mixes, we observe a gradual  
413 increase of  $U_{xR}$  and  $U_{xL}$  with time, and negligible  $U_y$  during most of the experiment  
414 duration (Fig. 8C, D). Suddenly at  $\sim 4000$ - $4500$  s,  $U_{xR}$  and  $U_{xL}$  strongly decrease and  
415  $U_y$  reaches a sharp peak; note that this coincides with the pressure drop, and we interpret  
416 this behavior as the result of failure of the overburden ahead of the intrusion. Note that  
417 the values of  $U_{xL}$  are higher than the values of  $U_{xR}$ . This suggests asymmetrical opening  
418 of the intrusion, but this may also be an artifact due to syrup flow along the glass. The  
419 latter is especially present in the experiments in 100% silica flour during the arrest  
420 phase of the dyke (see Fig. 3D).

421 In all experiments, the average displacements started growing only after the  
422 pressure reached its peak (Fig. 8). For higher cohesion experiments, this seems to  
423 coincide with the end of the initial pressure peak, i.e. after the first pressure drop. The  
424 second pressure drop in the higher cohesion experiments is associated with substantial  
425 uplift, after which most displacements cease.

426 To complement the average displacements, we extract the maximum  
427 incremental horizontal and vertical displacements (Fig. 8; central and right columns).  
428 All experiments show initial large horizontal displacements, as the intrusion initiates,  
429 followed by a decrease (Fig. 8). In the experiments with 90/10 and 80/20 hosts, the  
430 maximum incremental displacements remain constant, until they increase as the

431 intrusion approaches the surface (Fig. 8A, B). In both low cohesion experiments, the  
432 maximum vertical uplift gradually accelerates as the intrusion rises through the model;  
433 the maximum vertical uplift then suddenly decreases after failure of the overburden  
434 occurs shortly before eruption.

435           In the 50/50 experiment, the maximum horizontal displacements exhibit a  
436 first peak at ~1000 s, followed by a low at ~1500 s, then followed by rapid increase  
437 leading to a stable value during vertical ascent of the intrusion (Fig. 8C). We also note  
438 that the left side is constantly opening more than the right side. Failure of the  
439 overburden is associated with large horizontal maximum displacements (Fig 8C; central  
440 column). Uplift throughout the experiment is generally low during most of the  
441 experiments except for isolated timesteps. It accelerates rapidly when the intrusion  
442 approaches the free surface and the overburden fails ahead of the intrusion (Fig 8C;  
443 right column).

444           The highest cohesion experiment, 0/100, displays high initial maximum  
445 horizontal displacements at ~1500 s, followed by a gradually decreasing trend as the  
446 intrusion propagates (Fig. 8D; central column). In similarity with the 50/50 experiment,  
447 asymmetrical opening is evident in the average displacement, where the left side is  
448 opening significantly more than the right side. However, the large difference in average  
449 displacement is not echoed in the maximum displacement. This suggests that the  
450 average displacement calculation may have been influenced by flow parallel to the  
451 glass. Maximum uplift is low during most of the experiment, except for patches  
452 occurring in the early stages of the experiment, whereas the major uplifts occurred only  
453 in the late stage (Fig. 8D; right column). Here, critical failure of the overburden occurs  
454 creating open fractures acting as fluid pathways to the surface (Fig. 3). We associate  
455 the final uplift and horizontal displacement peaks to the uplifting of a block at the  
456 surface (Fig. 3).

457

## 458 **Interpretation: emplacement mechanisms**

459 Our results suggest that host cohesion plays a significant effect on the emplacement  
460 mechanics of the intrusion of a viscous fluid. At least two significantly differing  
461 emplacement mechanisms can be identified for the high and low cohesion hosts. In the  
462 following section we will interpret each set of experiments

463

464 *Emplacement mechanism in the 50GB/50SF high cohesion experiments*

465 For 50GB/50SF experiments, prominent planar sheet intrusions formed (Fig. 3C). The  
466 intrusion tip was generally narrow and sharp. During intrusion at depth, i.e. below the  
467 *critical depth*, there was very little or no uplift (Fig. 6C). Concurrently, a horizontal  
468 displacement halo could be observed indicating opening and minor compaction of the  
469 material along the fracture (Fig. 5C). The opening of the fracture appears to be slightly  
470 asymmetrical with one side opening more than the other (Fig. 8 C). The zone around  
471 and ahead of the fracture tip displays intermittent shear bands suggesting that the  
472 vertical sheet intrusions are propagating through both opening of the fracture and  
473 pushing ahead of the fracture tip (Fig. 7C). Pressure monitoring shows that the higher  
474 cohesion experiments (both 50/50 and 0/100) after the initial pressure peak, exhibited  
475 a significant pressure drop and a subsequent gradual pressure increase during vertical  
476 propagation. The initial pressure peak and subsequent drop, exhibit similar pressure  
477 behavior to that seen of hydraulic fractures [cf. *Murdoch*, 2002]. Finally, the intrusion  
478 of the sheet occurred step-wise, by arrested episodes of widening followed by transient  
479 bursts of propagation as seen in the propagation velocity (Fig. 4C). Some of these  
480 observations match well with that of hydraulic fractures such as the pressure curve and  
481 the sharp and narrow shape of the intrusion. However, the shear bands ahead of the tip  
482 and minor compaction of the host indicate non negligible plastic deformation playing  
483 an important role in the emplacement mechanics. Thus, we conclude that the syrup in  
484 the 50GB/50SF experiment was emplaced through a combined mechanism of dyke  
485 opening and widening along the entire walls and pushing ahead at the tip.  
486

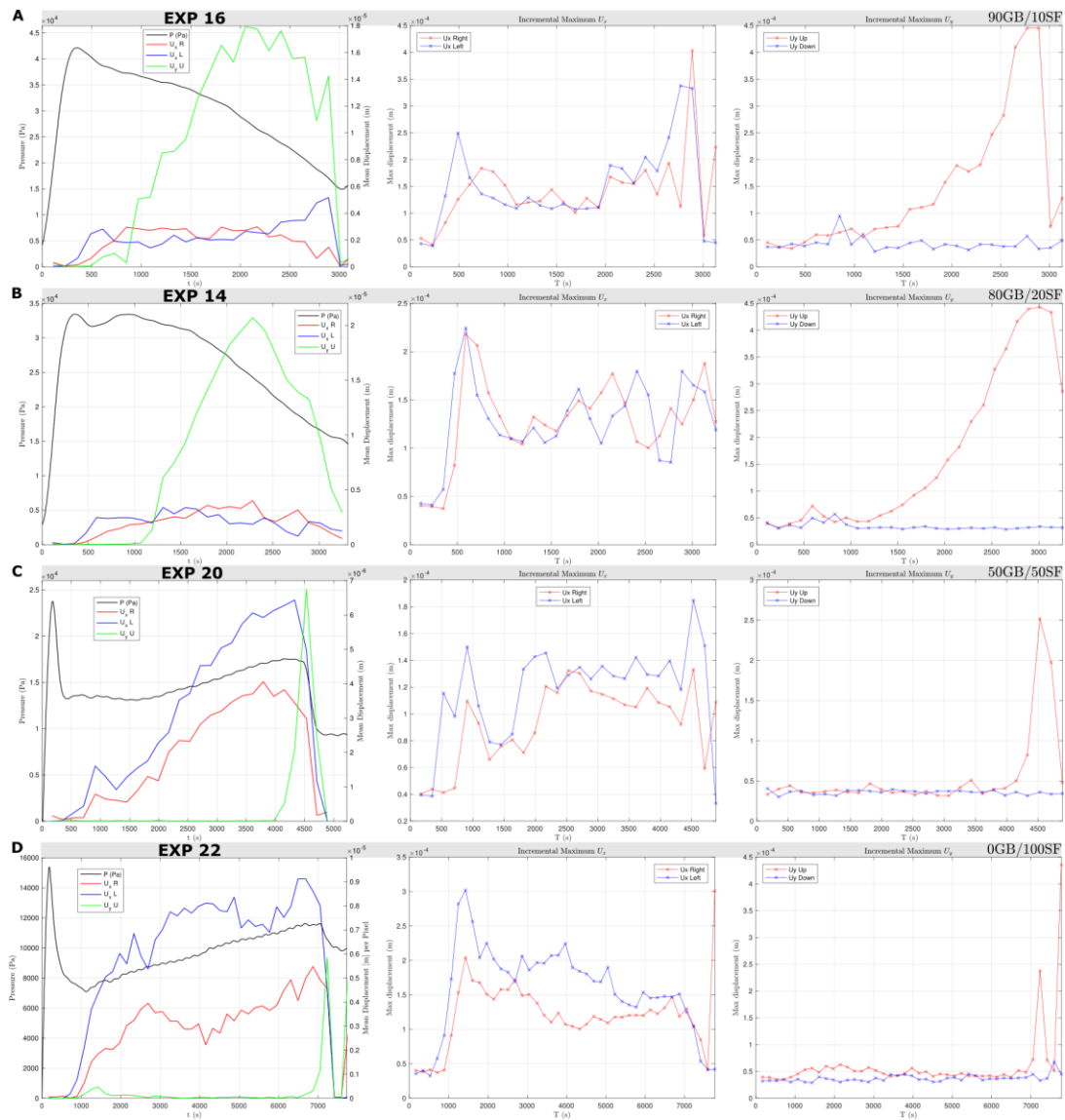


**Figure 8.** *Left column* Pressure and average displacement plots for 90/10 (A), 80/20 (B), 50/50 (C) and 0/100 (D). The black line shows pressure associated with the left axis. Blue and red lines are left and right average displacements, respectively and green shows upward average displacement associated with the right axis. Plots of additional experiments are available in the supplemental material S2. *Center and right column* Incremental maximum displacements in the left column for left (blue) and right (red) and in the right column for displacements upward (red) and downward (blue). Plots of additional experiments are available in the supplemental material S2.

487

488

489 *Emplacement mechanism in the 0GB/100SF high cohesion experiments*

490 The data monitored of the highest cohesion experiment (0/100) match well with that of

491 the 50/50 experiment except that it showed significant signs of compaction during

492 propagation at depth. All other experiments showed a quasi-constant maximum lateral

493 opening of the host during vertical propagation (Fig. 8 middle column). This was not  
494 the case for the 100% silica flour that showed an initial large maximum opening that  
495 gradually decreased (Fig. 8D middle column). The tip of the intrusion approached a  
496 standstill at the *critical depth* during which the intrusion dilated and opened until finally  
497 failing the overburden (Fig 4). It seems plausible therefore that compaction of the host  
498 played a role in temporarily arresting or stalling the intrusion in favor of dilation rather  
499 than upward propagation increasing the overall duration of the experiment. The role of  
500 compaction or an effective strain hardening in association with magma emplacement  
501 has not been greatly studied but has been proposed to play a non-significant role  
502 [Summer and Ayalon, 1995; Schmiedel et al., 2017b]. Similarly to the 50GB/50SF  
503 experiments, the syrup was emplaced through a combined mechanism of dyke opening  
504 and widening along the entire walls and pushing ahead at the tip. In addition, the dyke  
505 widening was accommodated by inelastic compaction of the host.

506

#### 507 *Emplacement mechanism in the 90GB/10SF low cohesion experiments*

508 The discontinuous nature of the intrusion in the 90GB/10SF experiment, visible in the  
509 experiment photographs (Fig. 3A), suggest a complex intrusion shape in the third  
510 dimension, i.e. a finger shape. This is confirmed when excavating the intrusion, which  
511 exhibits a finger-like tubular shape. The time series of vertical deformation show that  
512 the intrusion is associated with significant uplift already when the intrusion was at depth  
513 (Fig. 6A). The uplift increases throughout the experiment until the intrusion reaches the  
514 *critical depth*, where the overburden fails. The in-plane horizontal deformation  
515 demonstrates that in low cohesion hosts, deformation is concentrated to the tip region  
516 during propagation at depth (Fig. 5A). The concentration of horizontal deformation to  
517 the tip is drastically different form that observed in the two higher cohesion experiments  
518 described above. When the *critical depth* is reached, horizontal deformation extends  
519 from the intrusion tip up until the surface. The analysis of shear deformation in the host  
520 revealed larger reverse shear zones ahead of the intrusion tip compared to high cohesion  
521 experiments (Fig. 7). This indicates that there is a significant component of pushing of  
522 the fluid ahead of the path in which it is propagating. However, the shear bands ahead  
523 of the tip become weaknesses that may act as precursors for the subsequent propagation  
524 of the intrusion [Pollard, 1973; Haug et al., 2017; Schmiedel et al., 2019]. This may  
525 explain the undulating nature of the intrusion. The pressure readings exhibit a very

526 different behavior than what was seen for high cohesion experiments (Fig. 8),  
527 suggesting a drastically different emplacement dynamics than hydraulic fracturing. The  
528 propagation velocity also indicates the low cohesion experiments to propagate in bursts.  
529 However, due to the aforementioned 3D-nature of the intrusion shape we must caution  
530 against interpreting this as definite evidence. I.e., it is not sure that we are at all times  
531 properly tracking the intrusion tip in these experiments and therefore we must consider  
532 this observation to be inconclusive. We conclude from these observations that the  
533 finger-shaped intrusions in the 90GB/10SF experiments result from a “viscous  
534 indenter” mechanism, i.e. the viscous magma makes its own space by pushing the host  
535 ahead, which fails dominantly in shear.

536

#### 537 *Emplacement mechanism in the 80GB/20SF low cohesion experiments*

538 The host material in the 80GB/20SF experiment has a slightly larger cohesion than that  
539 in the 90GB/10SF experiment. This experiment overall exhibits many of the same  
540 characteristics as the previous low cohesion experiment (Figs. 3, 5-8). However, due to  
541 the higher cohesion the intrusion initially formed a sheet intrusion at the base of the  
542 model and transitions into a finger shaped intrusion (Fig. 3B). Fig. 5B Left shows this  
543 transition occurring with a horizontal displacement halo occurring simultaneously as  
544 there are lobes of horizontal deformation focused to the tip. Subsequent timesteps,  
545 below the *critical depth*, only show horizontal deformation focused to the intrusion tip.  
546 Similarly, Fig. 8B Left displays a brief low amplitude pressure drop followed by a  
547 transient pressure increase similarly to that of the higher cohesion experiments but then  
548 transitions into the linearly decreasing pressure displayed in the 90/10 experiment. We  
549 believe this to be associated with the sheet intrusion at the base of the intrusion and the  
550 transitions into a finger intrusion associated with pressure dropping as it propagates  
551 towards the surface. We therefore consider the 80/20 experiment to be a hybrid  
552 intrusion and an interesting look into the transition from one emplacement mechanism  
553 to another.

554

#### 555 *Emplacement mechanisms above the critical depth*

556 In all experiments, a clear transition happens at a few centimeters depth, referred to as  
557 the *critical depth*. Here, rapid uplift occurs associated with failure of the overburden  
558 and a change in the emplacement mechanism for both lower and higher cohesion

559 experiments. *Abdelmalak et al.* [2012] and *Poppe et al.* [2019], who similarly observed  
560 this shallow mechanism, showed that when the dyke tip is shallow enough, it is more  
561 favorable to lift up the overburden, which entire fails along shear bands from the dyke  
562 tip to the surface. This is supported by the sudden pressure drop happening when the  
563 dyke lifts up the overburden at the critical depth. This mechanism illustrates how the  
564 damage created ahead of the intrusion has the potential to act as weaknesses and  
565 mechanical precursors for the intrusion to utilize and intrude into [e.g. *Haug et al.*,  
566 2017; *Schmiedel et al.*, 2019].

567

### 568 *Summary - Emplacement mechanisms below the critical depth*

569 Below the critical depth, we document two types of emplacement mechanics depending  
570 on host cohesion. (1) For low cohesion hosts, a finger-shaped intrusion formed as a  
571 viscous indenter. In this mechanism, the intrusion tip pushes its host ahead, and the  
572 opening of the intrusion only focuses near the tip. (2) For high cohesion hosts, a sheet  
573 intrusion formed as a fracture. In this mechanism, the intrusion thickens by opening  
574 along its entire length, and the tip propagates by intermittent local opening and pushing  
575 of the host with a horizontal deformation halo surrounding the entire opening fracture  
576 (Fig. 9). These two emplacement mechanisms exhibited distinctly different pressure  
577 behavior, illustrating distinct emplacement dynamics. Both emplacement mechanisms  
578 were associate with shear bands. The shear bands were larger in areal extent as well as  
579 magnitude for the lower cohesion experiments. The shear bands were intermittent in  
580 high cohesion hosts and associated with upward propagation of the intrusion while they  
581 appeared more continuous for the lower cohesion experiments. Our experiments  
582 evidence the great role of host rock cohesion on the dynamics of emplacement of  
583 viscous liquids in Mohr-Coulomb hosts. Especially, our experiments show that sheets  
584 intrusions are favored in high-cohesion hosts whereas finger-shaped intrusions are  
585 favored in low-cohesion hosts.

586

## 587 **Discussion**

588

### 589 *Experimental constraints*

590 The experiments presented in this article use model host rocks made of compacted  
591 cohesive mixes of silica flour and glass beads. Such materials fail according to Mohr-

592 Coulomb criterion similar to rocks found in the shallow crust [Jaeger *et al.*, 2009]. Due  
593 to its cohesiveness, the 100% silica flour withstands non-negligible elastic stresses, as  
594 it sustains vertical walls under the load of its own weight [Abdelmalak *et al.*, 2016;  
595 *Guldstrand et al.*, 2017]. Conversely, pure glass beads collapse under their own weight  
596 and are close to cohesionless [Galland *et al.*, 2006; Abdelmalak *et al.*, 2016; Schmiedel  
597 *et al.*, 2017b]. In addition, the 100% silica flour exhibits a higher friction coefficient  
598 than the 100% glass beads. Therefore, we can fine-tune and study the effect of cohesion  
599 and friction on intrusion experiments by using mixes of these two materials  
600 [Abdelmalak *et al.*, 2016; Schmiedel *et al.*, 2017b]. The presented experiments are the  
601 first ones that investigate systematically the effect of rock cohesion and friction on the  
602 emplacement of dykes.  
603

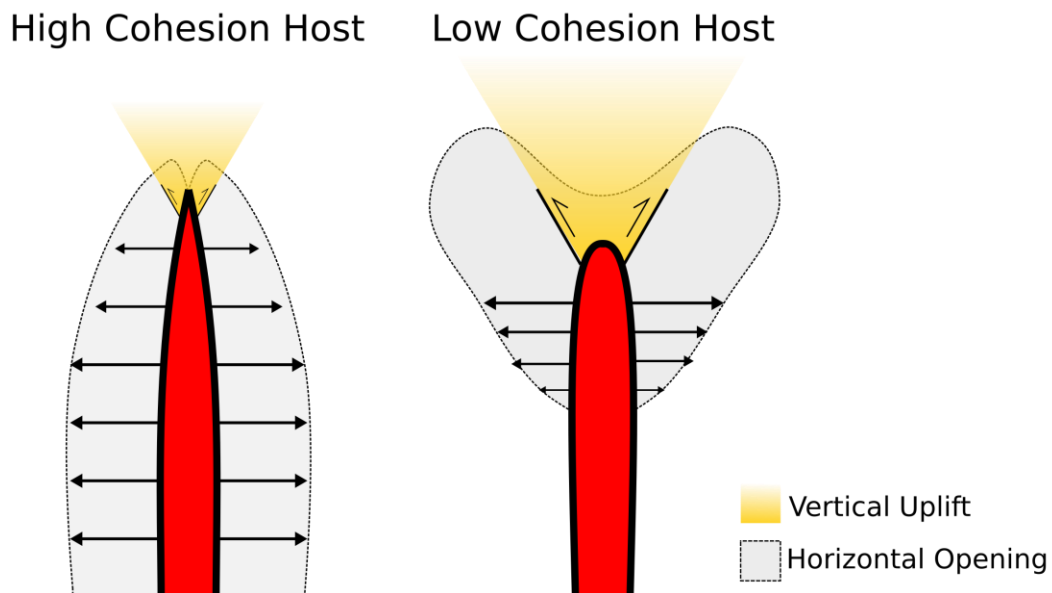


**Figure 9.** Interpretative sketch of the emplacement mechanics at play in high cohesion experiments (right) and low cohesion experiments (left). Shaded grey area denotes areas of horizontal deformation.

604

605

606            However, these materials and the experiment setup include some  
607 limitations. First, our experiments are homogeneous, i.e. without layering. Second, they  
608 assume lithostatic stress and do not account for the influence of tectonic stresses or  
609 stresses due to topography. Additionally, the use of granular Mohr-Coulomb materials  
610 do not allow for quantifying and extracting the elastic and plastic deformation  
611 separately [Guldstrand *et al.*, 2017].

612           The 2D Hele-Shaw cell ideally intends to simulate 2D processes in plain  
613 strain configuration, however in practice this is not the case. First, the friction of the  
614 granular materials along the glass walls trigger 3D stress distributions within the  
615 models. Second, in the low cohesion experiments, the intrusions cannot be considered  
616 strictly 2D as they consist of finger intrusions that appear disconnected on the  
617 observation plane, but connected in the third dimension. Nevertheless, the displacement  
618 maps and videos (supplemental material S2) show that the deformation monitored  
619 correlates well with the extracted intrusion from the experiment photos such that we  
620 are confident that we are tracking relevant deformation to the respective intrusions.

621           The tracking of the intrusion tip revealed significant advances in  
622 propagation to occur in bursts. This was more evident for lower cohesion hosts than in  
623 higher cohesion hosts, such that the average propagation velocity was higher in hosts  
624 of lower cohesions and lower in hosts of higher cohesions. Admittedly there are  
625 limitations in tracking the tip in the initial and final times of the experiments and in  
626 lower cohesion experiments as we may have more 3D effects in these experiments  
627 where we cannot track the tip of the intrusion. This means that we cannot strictly  
628 consider the observed burst dynamics to be strictly linked to emplacement mechanism  
629 for low cohesion experiments.

630           One may attribute the differing sheet and finger intrusion emplacement  
631 mechanisms and pressure readings to buoyancy. By just comparing densities, the syrup  
632 is indeed positively buoyant compared to the low cohesion glass beads and negatively  
633 buoyant compared to the high cohesion silica flour (see Table 1). However, we  
634 performed further analysis that show that the pressure within the syrup, when corrected  
635 for stresses due to viscous pipe flow and buoyancy, still remain significantly higher  
636 than the lithostatic stress for a given depth for all but one of the experiments into 100%  
637 silica flour (cf. supplemental material S3). This was calculated by taking the difference  
638 between the pressure readings and the hydrostatic stress of the fluid at a given tip depth  
639 and the viscous stress due to pipe flow when entering the setup (calculated through the  
640 Hagen-Poiseuille equation). This was compared to the lithostatic stress and the  
641 expected stress perpendicular to the dyke at a given depth. No interaction was observed  
642 between these pressure curves in all but one experiment (100% silica flour). In addition,  
643 the differences between the high-cohesion and low-cohesion experiments were  
644 noticeable already in the very early phases of the experiments, i.e. when the intrusions

645 were small and so the buoyancy effects negligible. We infer that in all experiments the  
646 effects of buoyancy were secondary and cannot explain the differences of pressure  
647 evolutions in the experiments.

648

#### 649 *The role of plastic deformation during magma emplacement in the brittle crust*

650 Our experiments highlight that small-scale (shear bands) and large-scale (compaction)  
651 plastic deformation can greatly control the propagation of sheet intrusions. In detail,  
652 our experiments show how local shear damage controls locally the propagation of the  
653 intrusion tips. Our laboratory results corroborate well (1) field observations of igneous  
654 fingers emplaced in low-strength rock [e.g. shale *Pollard et al.*, 1975; *Spacapan et al.*,  
655 2017; *Galland et al.*, 2019] and elasto-plastic numerical models [*Haug et al.*, 2017;  
656 *Haug et al.*, 2018; *Souche et al.*, 2019], which evidence how local plastic damage at the  
657 tip of propagating intrusions trigger weaknesses favorable to the subsequent  
658 propagation of the magma. Our experimental results provide a viable alternative  
659 mechanism to the widely established models of sheet intrusion emplacement, which  
660 assume intrusion propagation by tensile failure through a purely elastic host. Further  
661 research is now necessary to constrain under which geological conditions elasticity- or  
662 plasticity-dominated emplacement of igneous sheet intrusions occur.

663

#### 664 *Sheets versus fingers - Implications for dike and sill emplacement in the brittle crust*

665 Our experiments evidence two drastically distinct emplacement mechanisms of a  
666 viscous fluid in Mohr-Coulomb hosts of varying cohesions and friction angles, and the  
667 resulting intrusions exhibit different shapes, i.e. continuous sheets with relatively sharp  
668 tips in high-cohesion hosts versus aligned fingers in low cohesion hosts (Fig. 3). The  
669 modes of deformation of the host accommodating the emplacement of the viscous  
670 liquid also differ, with significantly more shear damage and failure in the low-cohesion  
671 hosts. Such difference has been proposed by *Galland et al.* [2014] on the basis of a  
672 scaling argument, and documented by *Poppe et al.* [2019].

673           The scaling argument of *Galland et al.* [2014], however, does not only  
674 involve the host cohesion, but it considers the mechanical coupling between the viscous  
675 stresses in the flowing liquid and the strength (i.e. cohesion) of the host rock. This  
676 scaling implies that when the viscous stresses dominate over the cohesive forces, the  
677 host rock deforms dominantly by shear failure. Our experiments corroborate well this

678 theoretical prediction, in agreement with the experiments of *Poppe et al.* [2019]. Our  
679 experiments show that not only the deformation mechanisms of the host differ, but also  
680 the emplacement dynamics of the liquid and the resulting intrusion shape.

681 Applied to geological systems, it predicts that fingers are expected to form  
682 preferably when the magma is highly viscous (e.g. andesitic to rhyolitic magmas)  
683 and/or when the host rock exhibits low cohesion (e.g. volcanic tuff, shale, poorly  
684 consolidated sandstones). Geological observations corroborate well this prediction.  
685 Igneous fingers observed in nature are often made of felsic magmas (andesitic to  
686 rhyolitic) [e.g. *Pollard et al.*, 1975; *Spacapan et al.*, 2017; *Galland et al.*, 2019] or were  
687 emplaced in very low strength host rock [*Duffield et al.*, 1986; *Schofield et al.*, 2012].  
688 Conversely, clear igneous sheets are common to mafic, i.e. low viscosity, magmas  
689 emplaced in relatively high cohesion host rock [e.g. *Gudmundsson*, 2020; *Poppe et al.*,  
690 2020]. Therefore, we expect that fingers form preferably at felsic volcanoes and/or in  
691 sedimentary basin settings whereas sheets form preferably at mafic volcanoes.

692 The overall shapes of the model intrusions differ: in the high-cohesion  
693 experiments, the sheets are continuous with sharp tips, whereas in low cohesion  
694 experiments the intrusions are made of aligned fingers with more blunt tips.  
695 Nevertheless, outcrop observations rarely provide exposures of entire intrusions, so that  
696 only short segments are observable. For instance, if only a short segment of a finger,  
697 without the tip, in our low-cohesion experiments was observable, one could easily  
698 extrapolate that the overall intrusion is a sheet. Thus, the overall inferred shape and  
699 emplacement mechanism of the observed intrusion would be incorrect. A field example  
700 illustrates this discussion point. The kilometer-scale outcrop studied by [*Galland et al.*,  
701 2019] exhibits an intrusion with an overall shape of a sill, however, it is made of a string  
702 of fingers. This interpretation was only possible because (1) the outcrop was large  
703 enough to display the gaps between the fingers and (2) the blunt tips and the  
704 surrounding structures in the host were exposed. If only the central part of a finger, with  
705 parallel top and bottom contacts, were exposed, or if the outcrop were discontinuous  
706 and did not expose the gaps between the fingers, one would naturally interpret this  
707 intrusion as being a sheet. Therefore, a local sheet shape is not conclusive to interpret  
708 the nature and the emplacement mechanism on intrusions. This example shows that  
709 intrusion-scale observations in addition to tip observations are necessary to infer the  
710 nature and emplacement mechanisms of intrusions in the brittle crust. It implies that

711 numerous dykes and sills have likely been interpreted as sheets, whereas they are strings  
712 of fingers, and their emplacement mechanisms are radically different.

713 Host rocks of volcanic plumbing systems in volcanic environments and in  
714 sedimentary basins are typically made of layers, the strength of which can vary  
715 considerably from competent (e.g., consolidated sandstone or crystalline rock) to  
716 weaker rock (e.g. volcanic tuff in volcanic environment of shale in sedimentary basins)  
717 [Ranalli, 1995; Galland *et al.*, 2018]. In the literature, the effects of the layering on  
718 magma emplacement has been addressed through static stress analysis resulting from  
719 stiffness contrast between the layers [Gudmundsson, 2020]. Yet so far the effect of this  
720 strength variation has only just started to be studied [Vachon and Hieronymus, 2016;  
721 Haug *et al.*, 2017; Schmiedel *et al.*, 2017a; Souche *et al.*, 2019]. Our experimental  
722 results suggest that the propagation mechanisms of an intrusion through layered crust  
723 may greatly vary from elasticity-dominated to plasticity-dominated depending on the  
724 local cohesion of the host rocks it propagates through, such that the propagation  
725 mechanism and dynamics may considerably vary from that of a sheet to that of a finger,  
726 and *vice versa*. Such variety of propagation mechanisms may explain why igneous sills  
727 and fingers tend to concentrate in low-strength host rock such as tuff and shale [e.g.  
728 Rodriguez Monreal *et al.*, 2009; Spacapan *et al.*, 2020]. Similarly, recent field studies  
729 in the Swedish and Norwegian Caledonides show that the emplacement of dykes can  
730 vary laterally and through time as the thermal state of the host vary [Kjøll *et al.*, 2019]:  
731 cold hosts behave competent and dykes are emplaced similarly to our high-cohesion  
732 experiments, but when the host rock gets hotter due to geodynamic processes, it can  
733 behave weak and dykes are emplaced similarly to our low-cohesion experiments. The  
734 close similarities between our experimental results and field observations strongly  
735 suggest that the lateral and temporal variations of inelastic properties of crustal rocks  
736 play a major role on the emplacement of igneous sheet intrusions.

737 Dyke arrest, i.e. the halting of vertical propagation of sheet intrusions, has often been  
738 attributed to the interaction with a more competent layer [Rivalta *et al.*, 2005;  
739 Gudmundsson, 2020], a weak interface [Kavanagh *et al.*, 2015; Kavanagh *et al.*, 2017]  
740 or due to reaching its neutral level of buoyancy [Hogan *et al.*, 1998; Taisne *et al.*, 2011].  
741 However, our experiments show that temporary halting of the model dykes can occur  
742 without layering and with constant magma influx. We infer from our experiments that  
743 the widening of the model dyke due to host compaction and cohesion may inhibit

744 vertical propagation, as the volume of the incoming magma is accommodated by dyke  
745 widening rather than by dyke lengthening.

746

#### 747 *Geophysical and geodetic implications*

748 The host deformation patterns accommodating dike and finger emplacement in our  
749 Mohr-Coulomb models do not match those predicted by static linear elastic model (e.g.  
750 Okada dislocation model). In all our experiments, only uplift above the propagating  
751 intrusions are observed [Figures 6 and 8; cf. *Guldstrand et al.*, 2017]. To date, there is  
752 no elastic geodetic model able to calculate only uplifting dome above a sub-vertical  
753 intrusion. For example, the elastic Okada model tends to produce two uplifting bulges  
754 delineated by a trough above, and aligned with, the orientation of the underlying sheet.  
755 However, symmetric and asymmetric doming has frequently been documented in  
756 nature [e.g. *Amelung et al.*, 2000; *Wright et al.*, 2006; *Jay et al.*, 2014], and the Okada  
757 model fails to interpret such data. Instead, these types of uplift are commonly modelled  
758 using inflating point sources or sub-horizontal inflating planar dislocations, despite the  
759 evidence of upward magma transport leading to eruption (e.g., *Sigmundsson et al.*,  
760 2010). Our experimental results suggest that surface doming can be interpreted as a  
761 result of dike emplacement controlled by the Coulomb properties of the crust. Such  
762 interpretation is corroborated by field observations of steeply dipping reverse faults  
763 associated with the emplacement of dykes in the shallow part of the crust, even in  
764 extensional settings [*Gudmundsson et al.*, 2008]. Therefore, our models show the  
765 limitation of the systematic use of elastic geodetic models to interpret geodetic signals  
766 monitored at active volcanoes, and strongly suggest that accounting for viscous flow  
767 [as already demonstrated by *Marsden et al.*, 2019] and Mohr-Coulomb host rheology  
768 are essential to understand magmatic systems and the deformation it produces.

769           Stepwise propagation, as demonstrated in our high cohesion experiments,  
770 implies that fast advances of the intrusion tip can happen over short periods of time.  
771 However, in between bursts, the tip may also advance smoothly. The burst propagation  
772 of the dyke in our experiments are in good agreement with the seismicity monitored  
773 during the 2014-2015 Bárðarbunga dyke intrusion, which revealed burst-like  
774 propagation [*Ágústsdóttir et al.*, 2016]. In addition, the seismicity at Bárðarbunga was  
775 not only active at the dyke tip but also remained active behind the interpreted dyke  
776 front. This observation is in good agreement with our high cohesion experiments, which

777 show that inelastic horizontal deformation affected the host over the entire fracture  
778 length, i.e., it is plausible that seismic activity would be active both at the dyke tip and  
779 below/behind the tip during intrusion.

780

781 *Implications for magma emplacement in felsic volcanoes and the formation of*  
782 *cryptodomes*

783 Our experiments aim to study volcanism in which the ratio of viscous stresses to  
784 cohesive stresses is non-negligible. This is more likely to be the case in areas with weak  
785 crust (such as in sedimentary basins or volcanic environments with pyroclastic  
786 deposits) and where there is felsic volcanism (i.e. high viscosity magma) [Galland *et*  
787 *al.*, 2014]. Sheet intrusions, such as dykes, are commonly thought to be associated with  
788 low viscosity resulting in thin sheets with sharp tips [e.g. Poppe *et al.*, 2020] however  
789 there are observations supporting high viscosity dykes to be more prolific than  
790 previously thought [Fink, 1985; Poland *et al.*, 2008]. These studies show that these  
791 sheet intrusions are generally thicker than their low-viscosity counterparts. This is in  
792 agreement with the thicker sheets produced in our experiments compared to gelatine-  
793 water models [Kavanagh *et al.*, 2018]. Moreover, we find that as cohesion decreases  
794 the sheets gets thinner and finally transitions into a finger-shaped intrusion similar in  
795 shape to andesitic sills observed in sedimentary basins [Spacapan *et al.*, 2017; Galland  
796 *et al.*, 2019]. The shapes of intrusions and associated strain patterns in our observations  
797 match very well with field observations of felsic sills emplaced in low strength/low  
798 friction shale. Overall, our experiments suggest that finger-shaped intrusions are likely  
799 essential elements of felsic magma transport.

800           The shallow emplacement of the syrup in our experiments exhibits  
801 characteristics of cryptodome emplacement, i.e. largely cylindrical or elongated bodies  
802 associated with uplift and planes of shear failure [Okada *et al.*, 1981; Donnadieu and  
803 Merle, 1998]. The emplacement of cryptodomes is a characteristic of another high-  
804 viscosity magma intrusions in the shallowest crust [e.g. Stewart and McPhie, 2003;  
805 Burchardt *et al.*, 2019]. The localized uplift and associated reverse fault planes in the  
806 latest stages of our experiments is in good agreement with uplift and semi-circular  
807 locations of seismicity at depth associated with the emplacement of a cryptodome at  
808 Usu volcano [Okada *et al.*, 1981; Tobita *et al.*, 2001]. Our experimental setup thus  
809 appears as a relevant tool for studying the dynamics of cryptodome emplacement.

810

## 811 **Conclusions**

812 In this study, we present quantitative laboratory experiments simulating the intrusion  
813 of viscous magma into host rock of varying cohesion, in order to quantify the effects of  
814 the Mohr-Coulomb properties of crustal rocks on the emplacement of planar intrusions.  
815 The main conclusions are as follows:

- 816 1. Continuous sheet intrusions form in high-cohesion hosts, whereas  
817 discontinuous finger-shaped intrusions form in low-cohesion hosts.
- 818 2. In all experiments, inelastic shear damage with, and uplift of, the host  
819 accommodate partly the emplacement of the model magma.
- 820 3. Sheet intrusions in high-cohesion hosts grow dominantly by dilation and  
821 opening along the entire length of the intrusion. In contrast, finger-shaped  
822 intrusions only thicken near the propagating tip of the intrusion.
- 823 4. The propagation of the fingers' tips is accommodated by significant shear  
824 damage bands, showing that the fingers dominantly propagate by pushing their  
825 host rock ahead, in agreement with the so-called *viscous indenter* model.  
826 Conversely, shear damage is much less prominent near the tip of sheet  
827 intrusions, which dominantly propagate like fractures.
- 828 5. In all experiments, when the intrusion tip reached a shallow critical depth, the  
829 overburden is pushed upward and fails along shear damage bands, which control  
830 the subsequent propagation of the model magma. This shallow emplacement  
831 mechanism is likely relevant for revealing the emplacement of cryptodomes in  
832 nature.
- 833 6. When magma is emplaced in layered host, like in sedimentary basins, it is likely  
834 that both emplacement mechanisms successively occur.
- 835 7. All in all, our experiments suggest that the Mohr-Coulomb properties of the  
836 crust must be systematically accounted in models of planar intrusion  
837 emplacement.

838

## 839 **Acknowledgements**

840 Guldstrand and Souche's position was funded by the DIPS project (grant no. 240467)  
841 from the Norwegian Research Council. Bertelsen's position was funded by the Faculty  
842 of Mathematics and Natural Sciences of the University of Oslo. The authors thank

843 Tobias Schmiedel & Marcel Moura for assistance in determining wetting by performing  
844 contact angle measurements. Regis Mourgues is acknowledged for assisting in setting  
845 up a guest researcher visit in Le Mans to study their experimental setup. The data  
846 presented in this study is available on demand.

847

## 848 **References**

- 849 Abdelmalak, M. M., R. Mourgues, O. Galland, and D. Bureau (2012), Fracture mode analysis and  
850 related surface deformation during dyke intrusion: Results from 2D  
851 experimental modelling, *Earth Planet. Sci. Lett.*, 359-360, 93-105.
- 852 Abdelmalak, M. M., C. Bulois, R. Mourgues, O. Galland, J. B. Legland, and C. Gruber (2016),  
853 Description of new dry granular materials of variable cohesion and friction  
854 coefficient: Implications for laboratory modeling of the brittle crust,  
855 *Tectonophysics*, 684, 39-51.
- 856 Ágústsdóttir, T., J. Woods, T. Greenfield, R. G. Green, R. S. White, T. Winder, B. Brandsdóttir, S.  
857 Steinthórsson, and H. Soosalu (2016), Strike - slip faulting during the 2014  
858 Bárðarbunga - Holuhraun dike intrusion, central Iceland, *Geophysical Research*  
859 *Letters*.
- 860 Amelung, F., S. Jónsson, H. Zebker, and P. Segall (2000), Widespread uplift and 'trapdoor' faulting  
861 on Galapagos volcanoes observed with radar interferometry, *Nature*, 407(6807),  
862 993-996.
- 863 Beckett, F., H. Mader, J. Phillips, A. Rust, and F. Witham (2011), An experimental study of low-  
864 Reynolds-number exchange flow of two Newtonian fluids in a vertical pipe,  
865 *Journal of Fluid Mechanics*, 682, 652-670.
- 866 Bunger, A. P., and A. R. Cruden (2011), Modeling the growth of laccoliths and large mafic sills:  
867 Role of magma body forces, *J. Geophys. Res.*, 116(B2), B02203.
- 868 Burchardt, S., T. Mattsson, J. O. Palma, O. Galland, B. Almqvist, K. Mair, D. A. Jerram, Ø. Hammer,  
869 and Y. Sun (2019), Progressive Growth of the Cerro Bayo Cryptodome,  
870 Chachahuén Volcano, Argentina—Implications for Viscous Magma  
871 Emplacement, *Journal of Geophysical Research: Solid Earth*, 124(8), 7934-7961.
- 872 Delcamp, A., B. v. W. de Vries, M. R. James, L. Gailler, and E. Lebas (2012), Relationships between  
873 volcano gravitational spreading and magma intrusion, *Bulletin of Volcanology*,  
874 74(3), 743-765.
- 875 Donnadieu, F., and O. Merle (1998), Experiments on the indentation process during cryptodome  
876 intrusions: new insights into Mount St. Helens deformation, *Geology*, 26(1), 79-  
877 82.
- 878 Duffield, W. A., C. R. Bacon, and P. T. Delaney (1986), Deformation of poorly consolidated  
879 sediment during shallow emplacement of a basalt sill, Coso Range, California,  
880 *Bull. Volcanol.*, 48(2), 97-107.

881 Fink, J. H. (1985), Geometry of silicic dikes beneath the Inyo Domes, California, *Journal of*  
882 *Geophysical Research: Solid Earth*, 90(B13), 11127-11133.

883 Galland, O., and J. Scheibert (2013), Analytical model of surface uplift above axisymmetric flat-  
884 lying magma intrusions: Implications for sill emplacement and geodesy, *J.*  
885 *Volcanol. Geotherm. Res.*, 253(0), 114-130.

886 Galland, O., P. R. Cobbold, E. Hallot, J. de Bremond d'Ars, and G. Delavaud (2006), Use of vegetable  
887 oil and silica powder for scale modelling of magmatic intrusion in a deforming  
888 brittle crust, *Earth Planet. Sci. Lett.*, 243, 786-804.

889 Galland, O., S. Burchardt, E. Hallot, R. Mourgues, and C. Bulois (2014), Dynamics of dikes versus  
890 cone sheets in volcanic systems, *Journal of Geophysical Research: Solid Earth*,  
891 2014JB011059.

892 Galland, O., H. S. Bertelsen, F. Guldstrand, L. Girod, R. F. Johannessen, F. Bjugger, S. Burchardt, and  
893 K. Mair (2016), Application of open-source photogrammetric software MicMac  
894 for monitoring surface deformation in laboratory models, *Journal of Geophysical*  
895 *Research: Solid Earth*.

896 Galland, O., J. B. Spacapan, O. Rabbal, K. Mair, F. G. Soto, T. Eiken, M. Schiuma, and H. A. Leanza  
897 (2019), Structure, emplacement mechanism and magma-flow significance of  
898 igneous fingers – Implications for sill emplacement in sedimentary basins, *J.*  
899 *Struct. Geol.*

900 Galland, O., et al. (2018), Storage and transport of magma in the layered crust-Formation of sills  
901 and related flat-lying intrusions, in *Volcanic and Igneous Plumbing Systems*,  
902 edited by S. Burchardt, pp. 111-136, Elsevier.

903 Gudmundsson, A. (2020), *Volcanotectonics: Understanding the Structure, Deformation and*  
904 *Dynamics of Volcanoes*, Cambridge University Press, Cambridge.

905 Gudmundsson, A., N. Friese, I. Galindo, and S. L. Philipp (2008), Dike-induced reverse faulting in a  
906 graben, *Geology*, 36(2), 123.

907 Guldstrand, F., S. Burchardt, E. Hallot, and O. Galland (2017), Dynamics of Surface Deformation  
908 Induced by Dikes and Cone Sheets in a Cohesive Coulomb Brittle Crust, *Journal*  
909 *of Geophysical Research: Solid Earth*, 122(10), 8511-8524.

910 Guldstrand, F., O. Galland, E. Hallot, and S. Burchardt (2018), Experimental Constraints on  
911 Forecasting the Location of Volcanic Eruptions from Pre-eruptive Surface  
912 Deformation, *Frontiers in Earth Science*, 6(7).

913 Halls, H. C., and W. F. Fahrig (Eds.) (1987), *Mafic dyke swarms*, 503 pp., Toronto, Canada.

914 Haug, Ø. T., O. Galland, P. Souloumiac, A. Souche, F. Guldstrand, and T. Schmiedel (2017), Inelastic  
915 damage as a mechanical precursor for the emplacement of saucer-shaped  
916 intrusions, *Geology*, 45(12), 1099-1102.

917 Haug, Ø. T., O. Galland, P. Souloumiac, A. Souche, F. Guldstrand, T. Schmiedel, and B. Maillot  
918 (2018), Shear versus tensile failure mechanisms induced by sill intrusions --  
919 Implications for emplacement of conical and saucer-shaped intrusions, *Journal*  
920 *of Geophysical Research: Solid Earth*, 123, 3430-3449.

921 Hogan, J. P., J. D. Price, and M. C. Gilbert (1998), Magma traps and driving pressure: consequences  
922 for pluton shape and emplacement in an extensional regime, *J. Struct. Geol.*,  
923 20(9-10), 1155-1168.

924 Jaeger, J. C., N. G. Cook, and R. Zimmerman (2009), *Fundamentals of rock mechanics*, John Wiley &  
925 Sons.

926 Jay, J., F. Costa, M. Pritchard, L. Lara, B. Singer, and J. Herrin (2014), Locating magma reservoirs  
927 using InSAR and petrology before and during the 2011–2012 Cordón Caulle  
928 silicic eruption, *Earth and Planetary Science Letters*, 395, 254-266.

929 Kavanagh, J. L., D. Boutelier, and A. R. Cruden (2015), The mechanics of sill inception, propagation  
930 and growth: Experimental evidence for rapid reduction in magmatic  
931 overpressure, *Earth Planet. Sci. Lett.*, 421(0), 117-128.

932 Kavanagh, J. L., B. D. Rogers, D. Boutelier, and A. R. Cruden (2017), Controls on sill and dyke-sill  
933 hybrid geometry and propagation in the crust: The role of fracture toughness,  
934 *Tectonophysics*, 698, 109-120.

935 Kavanagh, J. L., A. J. Burns, S. Hilmi Hazim, E. P. Wood, S. A. Martin, S. Hignett, and D. J. C. Dennis  
936 (2018), Challenging dyke ascent models using novel laboratory experiments:  
937 Implications for reinterpreting evidence of magma ascent and volcanism, *J.*  
938 *Volcanol. Geotherm. Res.*, 354, 87-101.

939 Kjøl, H. J., O. Galland, L. Labrousse, and T. B. Andersen (2019), Emplacement mechanisms of a  
940 dyke swarm across the brittle-ductile transition and the geodynamic  
941 implications for magma-rich margins, *Earth and Planetary Science Letters*, 518,  
942 223-235.

943 Llewellyn, E., H. Mader, and S. Wilson (2002), The rheology of a bubbly liquid, paper presented at  
944 Proceedings of the Royal Society of London A: Mathematical, Physical and  
945 Engineering Sciences, The Royal Society.

946 Magee, C., et al. (2016), Lateral magma flow in mafic sill complexes, *Geosphere*, 12(3), 809-841.

947 Marsden, L. H., J. W. Neuberg, M. E. Thomas, P. A. Mothes, and M. C. Ruiz (2019), Combining  
948 Magma Flow and Deformation Modeling to Explain Observed Changes in Tilt,  
949 *Frontiers in Earth Science*, 7, 219.

950 Mart, Y., and O. Dauteuil (2000), Analogue experiments of propagation of oblique rifts,  
951 *Tectonophysics*, 316(1-2), 121-132.

952 Mathieu, L., B. v. W. de Vries, E. P. Holohan, and V. R. Troll (2008), Dykes, cups, saucers and sills:  
953 Analogue experiments on magma intrusion into brittle rocks, *Earth and*  
954 *Planetary Science Letters*, 271(1), 1-13.

955 Murdoch, L. C. (2002), Mechanical analysis of idealized shallow hydraulic fracture, *Journal of*  
956 *Geotechnical and Geoenvironmental Engineering*, 128(6), 488-495.

957 Okada, H., H. Watanabe, H. Yamashita, and I. Yokoyama (1981), Seismological significance of the  
958 1977–1978 eruptions and the magma intrusion process of Usu volcano,  
959 Hokkaido, *Journal of volcanology and geothermal research*, 9(4), 311-334.

960 Poland, M. P., W. P. Moats, and J. H. Fink (2008), A model for radial dike emplacement in  
961 composite cones based on observations from Summer Coon volcano, Colorado,  
962 USA, *Bulletin of Volcanology*, 70(7), 861-875.

963 Pollard, D. D. (1973), Derivation and evaluation of a mechanical model for sheet intrusions,  
964 *Tectonophysics*, 19(3), 233-269.

965 Pollard, D. D. (1987), Elementary fracture mechanics applied to the structural interpretation of  
966 dikes, in *Mafic dyke swarms*, edited by H. C. Halls and W. F. Fahrig, pp. 5-24, Geol.  
967 Assoc. Canada Spec. Pap.

968 Pollard, D. D., O. H. Muller, and D. R. Dockstader (1975), The Form and Growth of Fingered Sheet  
969 Intrusions, *Geol. Soc. Am. Bull.*, 86(3), 351-363.

970 Poppe, S., O. Galland, N. J. de Winter, S. Goderis, P. Claeys, V. Debaille, P. Boulvais, and M. Kervyn  
971 (2020), Structural and Geochemical Interactions Between Magma and  
972 Sedimentary Host Rock: The Hovedøya Case, Oslo Rift, Norway, *G3*, 21(3),  
973 e2019GC008685.

974 Poppe, S., et al. (2019), An inside perspective on magma intrusion: quantifying 3D displacement  
975 and strain in laboratory experiments by dynamic X-Ray computed tomography,  
976 *Frontiers in Earth Science*, 7.

977 Rabbel, O., O. Galland, K. Mair, I. Lecomte, K. Senger, J. B. Spacapan, and R. Manceda (2018), From  
978 field analogues to realistic seismic modelling: a case study of an oil-producing  
979 andesitic sill complex in the Neuquén Basin, Argentina, *Journal of the Geological*  
980 *Society*, jgs2017-2116.

981 Ranalli, G. (1995), *Rheology of the Earth*, Springer Science & Business Media.

982 Rivalta, E., M. Böttlinger, and T. Dahm (2005), Buoyancy-driven fracture ascent: Experiments in  
983 layered gelatine, *J. Volcanol. Geotherm. Res.*, 144, 273-285.

984 Rivalta, E., B. Taisne, A. P. Bungler, and R. F. Katz (2015), A review of mechanical models of dike  
985 propagation: Schools of thought, results and future directions, *Tectonophysics*,  
986 638, 1-42.

987 Rodriguez Monreal, F., H. J. Villar, R. Baudino, D. Delpino, and S. Zencich (2009), Modeling an  
988 atypical petroleum system: A case study of hydrocarbon generation, migration  
989 and accumulation related to igneous intrusions in the Neuquén Basin, Argentina,  
990 *Mar. Pet. Geol.*, 26(4), 590-605.

991 Rosu, A.-M., M. Pierrot-Deseilligny, A. Delorme, R. Binet, and Y. Klinger (2015), Measurement of  
992 ground displacement from optical satellite image correlation using the free  
993 open-source software MicMac, *ISPRS J. Photogram. Rem. Sens.*, 100(0), 48-59.

994 Rupnik, E., M. Daakir, and M. Pierrot Deseilligny (2017), MicMac – a free, open-source solution for  
995 photogrammetry, *Open Geospatial Data, Software and Standards*, 2(1), 14.

996 Schmiedel, T., O. Galland, and C. Breitzkreuz (2017a), Dynamics of sill and laccolith emplacement  
997 in the brittle crust: role of host rock strength and deformation mode, *Journal of*  
998 *Geophysical Research: Solid Earth*, 122(11), 8625-9484.

999 Schmiedel, T., O. Galland, Ø. T. Haug, G. Dumazer, and C. Breitzkreuz (2019), Coulomb failure of  
 1000 Earth's brittle crust controls growth, emplacement and shapes of igneous sills,  
 1001 saucer-shaped sills and laccoliths, *Earth Planet. Sci. Lett.*, 510, 161-172.  
 1002 Schmiedel, T., S. Kjoberg, S. Planke, C. Magee, O. Galland, N. Schofield, C. A.-L. Jackson, and D. A.  
 1003 Jerram (2017b), Mechanisms of overburden deformation associated with the  
 1004 emplacement of the Tulipan sill, mid-Norwegian margin, *Interpretation*, 5(3),  
 1005 SK23-SK38.  
 1006 Schofield, N., D. J. Brown, C. Magee, and C. T. Stevenson (2012), Sill morphology and comparison  
 1007 of brittle and non-brittle emplacement mechanisms, *J. Geol. Soc. London*, 169(2),  
 1008 127-141.  
 1009 Senger, K., J. Millett, S. Planke, K. Ogata, C. H. Eide, M. Festøy, O. Galland, and D. A. Jerram (2017),  
 1010 Effects of igneous intrusions on the petroleum system: a review, *First Break*,  
 1011 35(6), 47-56.  
 1012 Souche, A., O. Galland, Ø. T. Haug, and M. Dabrowski (2019), Impact of host rock heterogeneity on  
 1013 failure around pressurized conduits: Implications for finger-shaped magmatic  
 1014 intrusions, *Tectonophysics*, 765, 52-63.  
 1015 Spacapan, J. B., O. Galland, H. A. Leanza, and S. Planke (2017), Igneous sill and finger emplacement  
 1016 mechanism in shale-dominated formations: a field study at Cuesta del Chihuido,  
 1017 Neuquén Basin, Argentina, *J. Geol. Soc. London*, 174(3), 422-433.  
 1018 Spacapan, J. B., A. D'Odorico, O. Palma, O. Galland, E. Rojas Vera, R. Ruiz, H. A. Leanza, A.  
 1019 Medialdea, and R. Manceda (2020), Igneous petroleum systems in the Malargüe  
 1020 fold and thrust belt, Río Grande Valley area, Neuquén Basin, Argentina, *Mar. Pet.*  
 1021 *Geol.*, 111, 309-331.  
 1022 Stewart, A. L., and J. McPhie (2003), Internal structure and emplacement of an Upper Pliocene  
 1023 dacite cryptodome, Milos Island, Greece, *Journal of Volcanology and Geothermal*  
 1024 *Research*, 124(1-2), 129-148.  
 1025 Summer, N. S., and A. Ayalon (1995), Dike intrusion into unconsolidated sandstone and the  
 1026 development of quartzite contact zones, *Journal of Structural Geology*, 17(7),  
 1027 997-1010.  
 1028 Taisne, B., S. Tait, and C. Jaupart (2011), Conditions for the arrest of a vertical propagating dyke,  
 1029 *Bulletin of Volcanology*, 73(2), 191-204.  
 1030 Tibaldi, A. (2015), Structure of volcano plumbing systems: A review of multi-parametric effects,  
 1031 *Journal of Volcanology and Geothermal Research*, 298, 85-135.  
 1032 Tobita, M., M. Murakami, H. Nakagawa, H. Yarai, S. Fujiwara, and P. A. Rosen (2001), 3 - D surface  
 1033 deformation of the 2000 Usu eruption measured by matching of SAR images,  
 1034 *Geophysical Research Letters*, 28(22), 4291-4294.  
 1035 Vachon, R., and C. F. Hieronymus (2016), Effect of host-rock rheology on dyke shape, thickness,  
 1036 and magma overpressure, *Geophysical Journal International*, ggw448.

1037 Wright, T. J., C. Ebinger, J. Biggs, A. Ayele, G. Yirgu, D. Keir, and A. Stork (2006), Magma-  
1038 maintained rift segmentation at continental rupture in the 2005 Afar dyking  
1039 episode, *Nature*, 442(7100), 291-294.

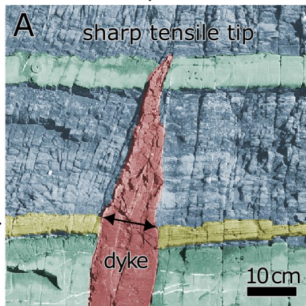
1040

1041

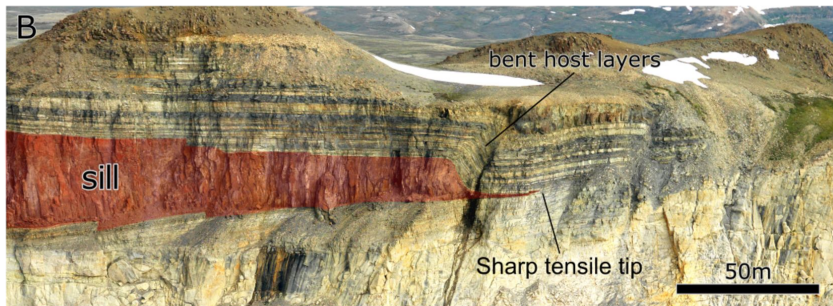
Figure 1.

### Dyke

Competent Host Rock



### Sill



Weak Host Rock

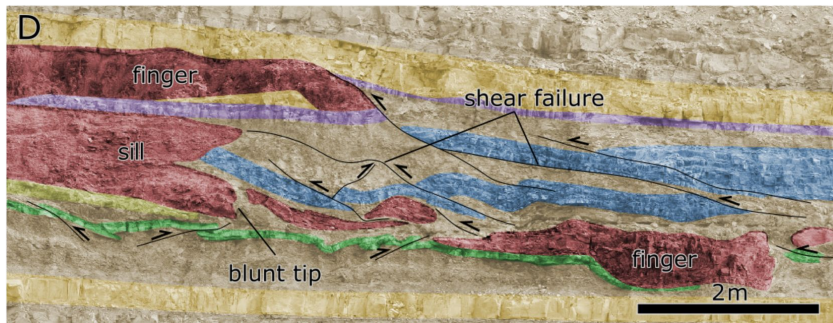
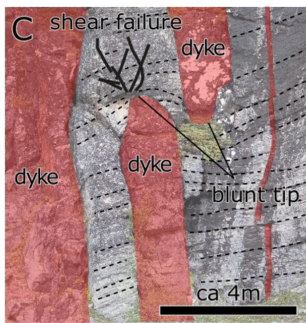


Figure 2.

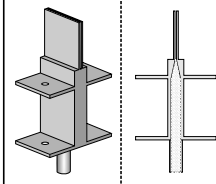
# Hele-Shaw Cell

800 mm

30 mm

## Inlet Closeup

Slit dimensions:  
30x1x30 mm



## Host Materials:

Glass Beads  
Silica Flour

## Texture:

Aluminum Silicate

500 mm

Golden Syrup

10 cm

Automated  
Syringe Pump  
0.5 mL/min

Pressure Sensor

DSLR  
Camera

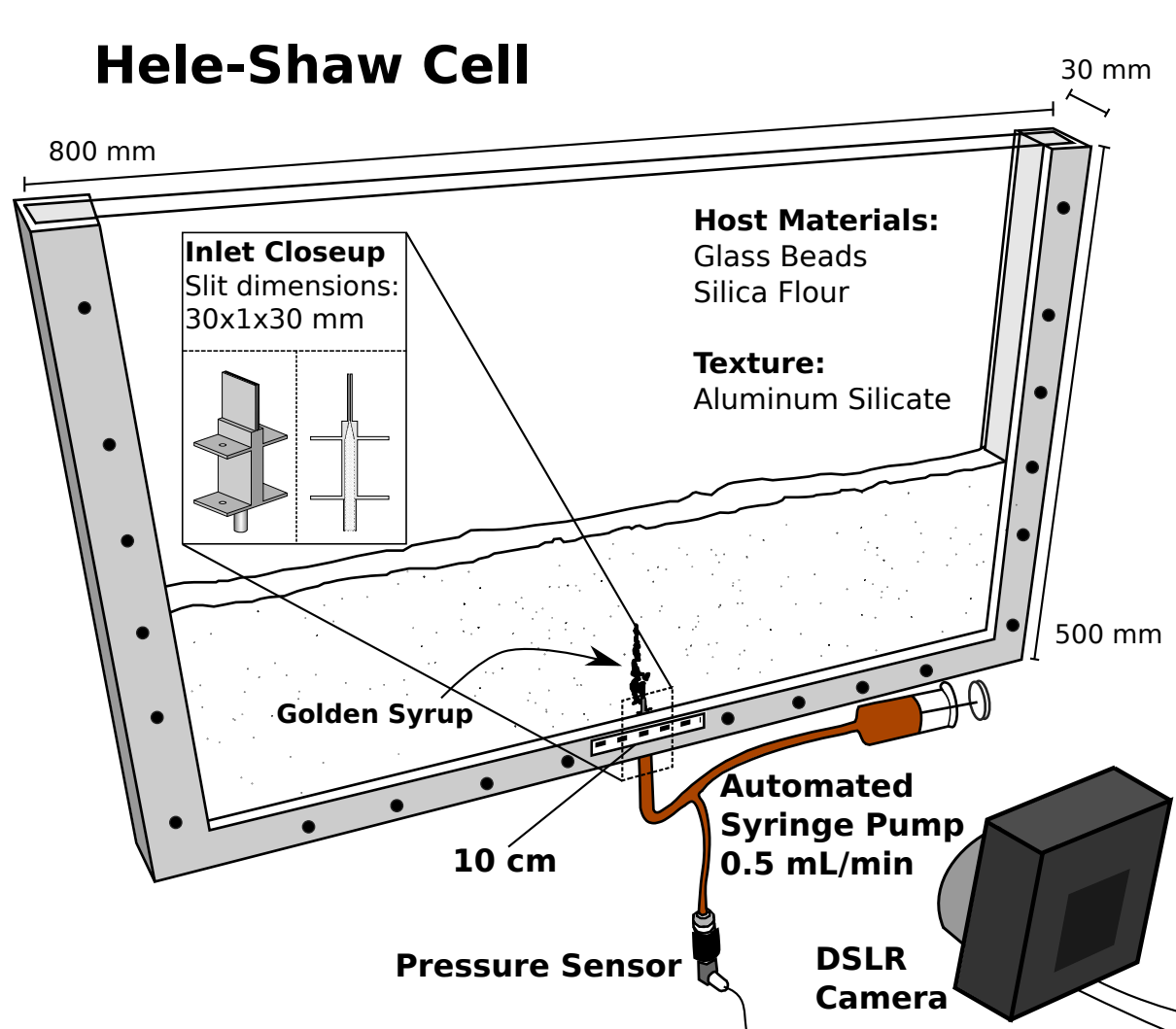
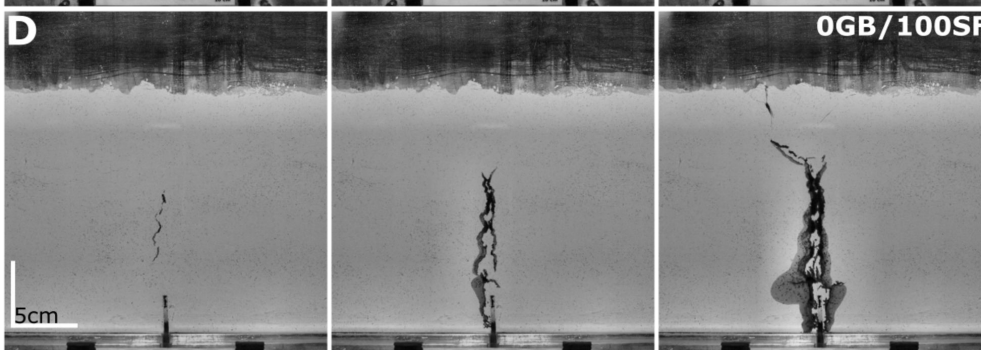
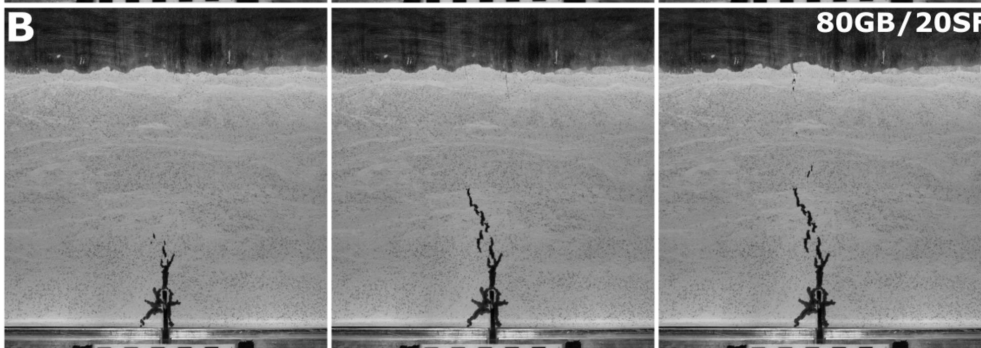
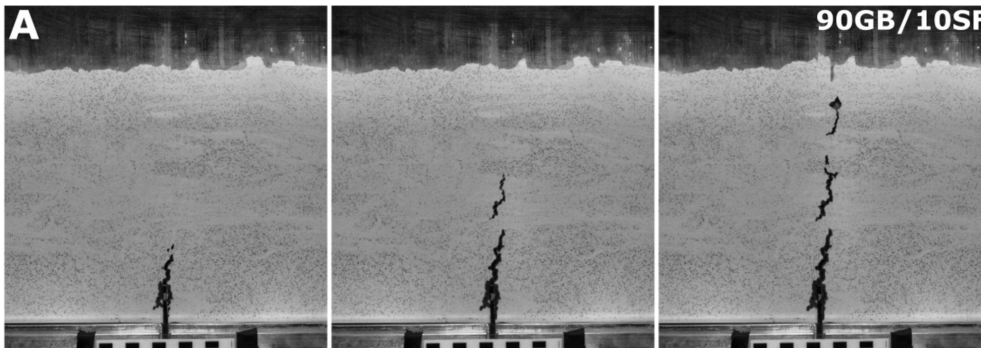


Figure 3.

Time

Finger



Sheet

Cohesion

5cm

**Figure 4.**

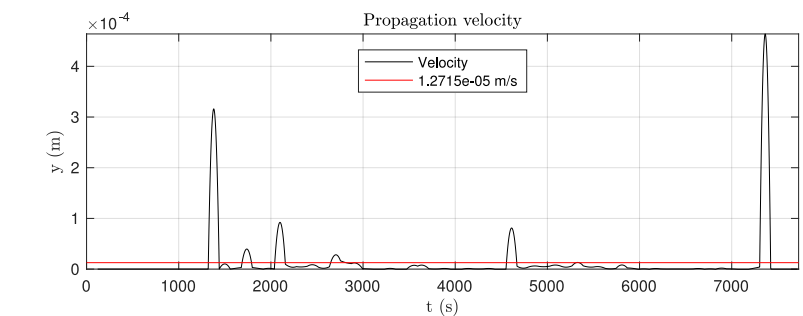
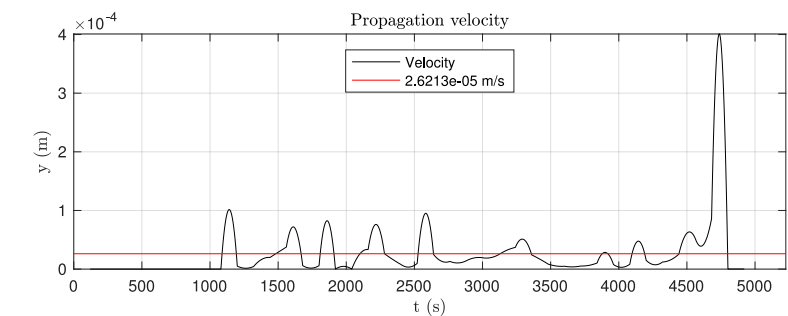
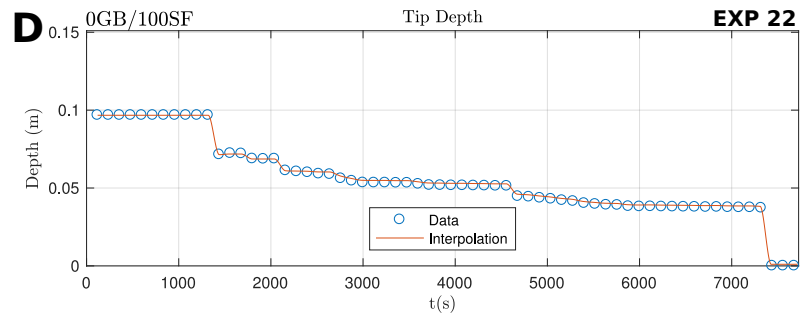
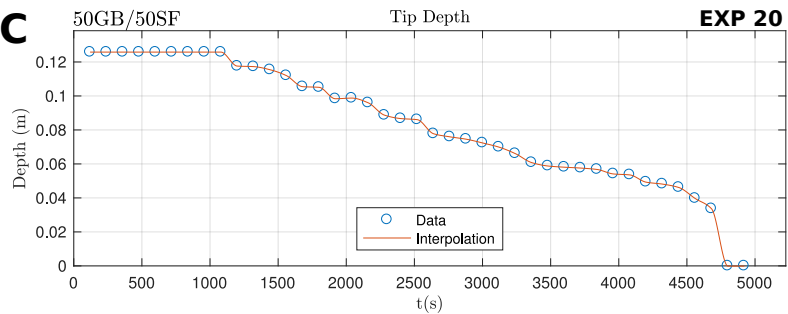
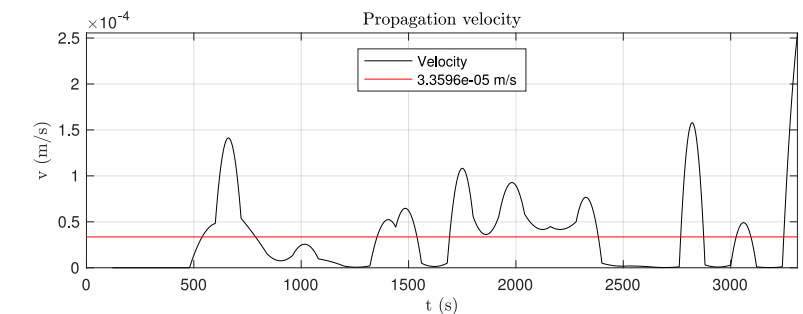
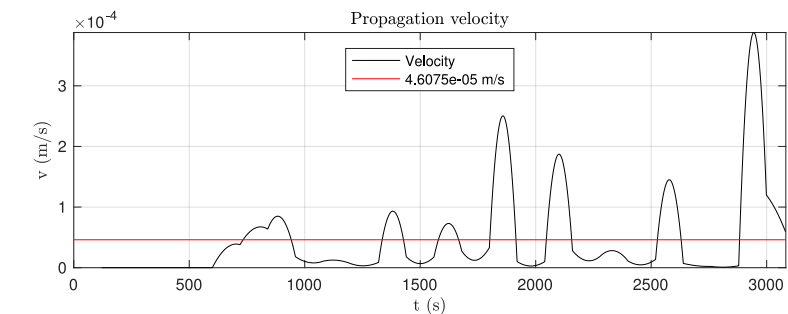
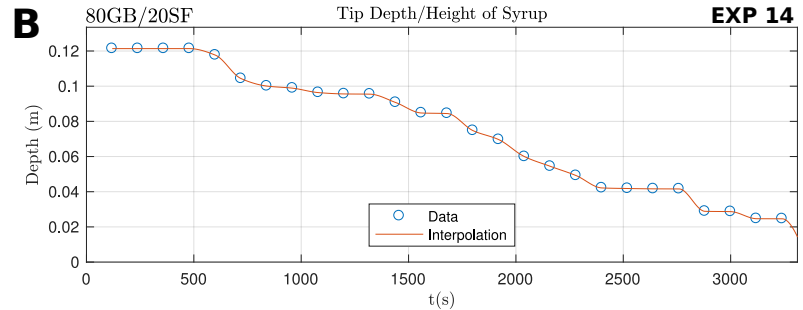
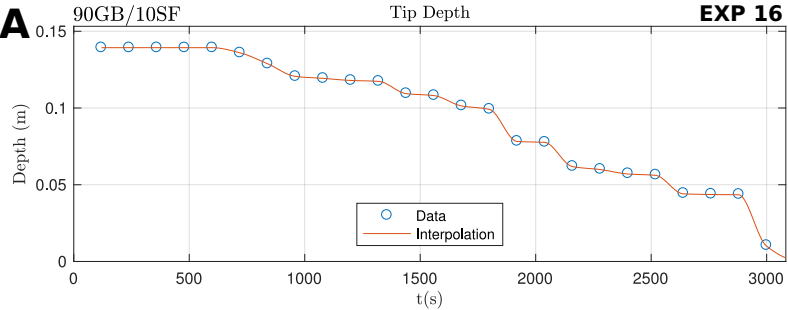


Figure 5.

# Horizontal Displacement

Time

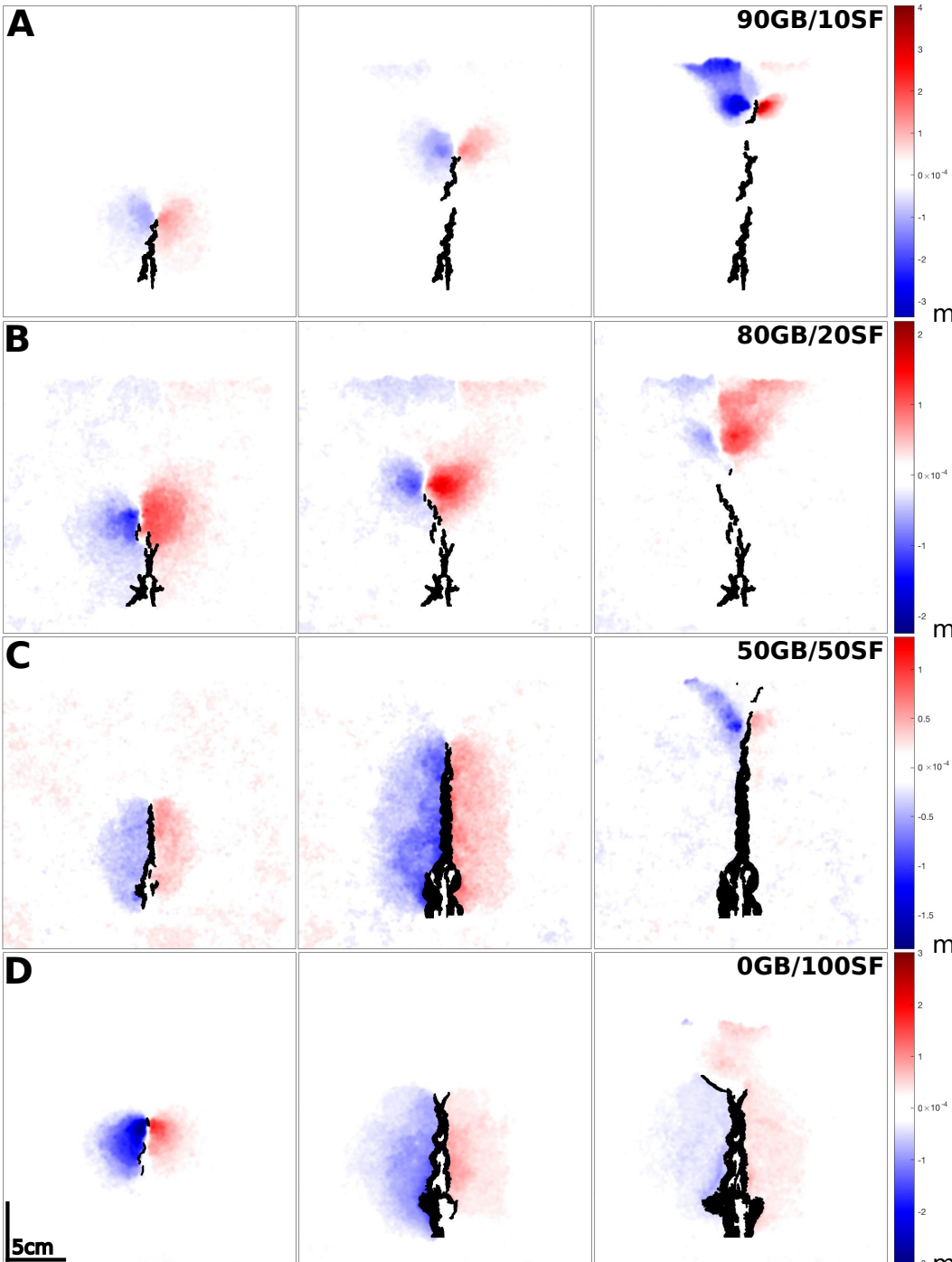


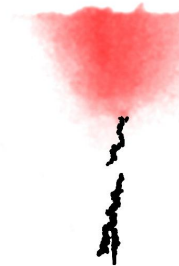
Figure 6.

# Vertical Displacement

Time

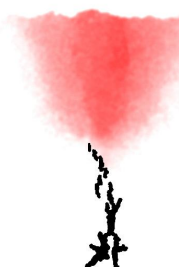
**A**

90GB/10SF



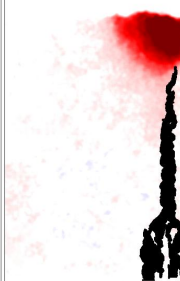
**B**

80GB/20SF



**C**

50GB/50SF



**D**

0GB/100SF



Cohesion

5cm

**Figure 7.**

# Shear Strain

Time

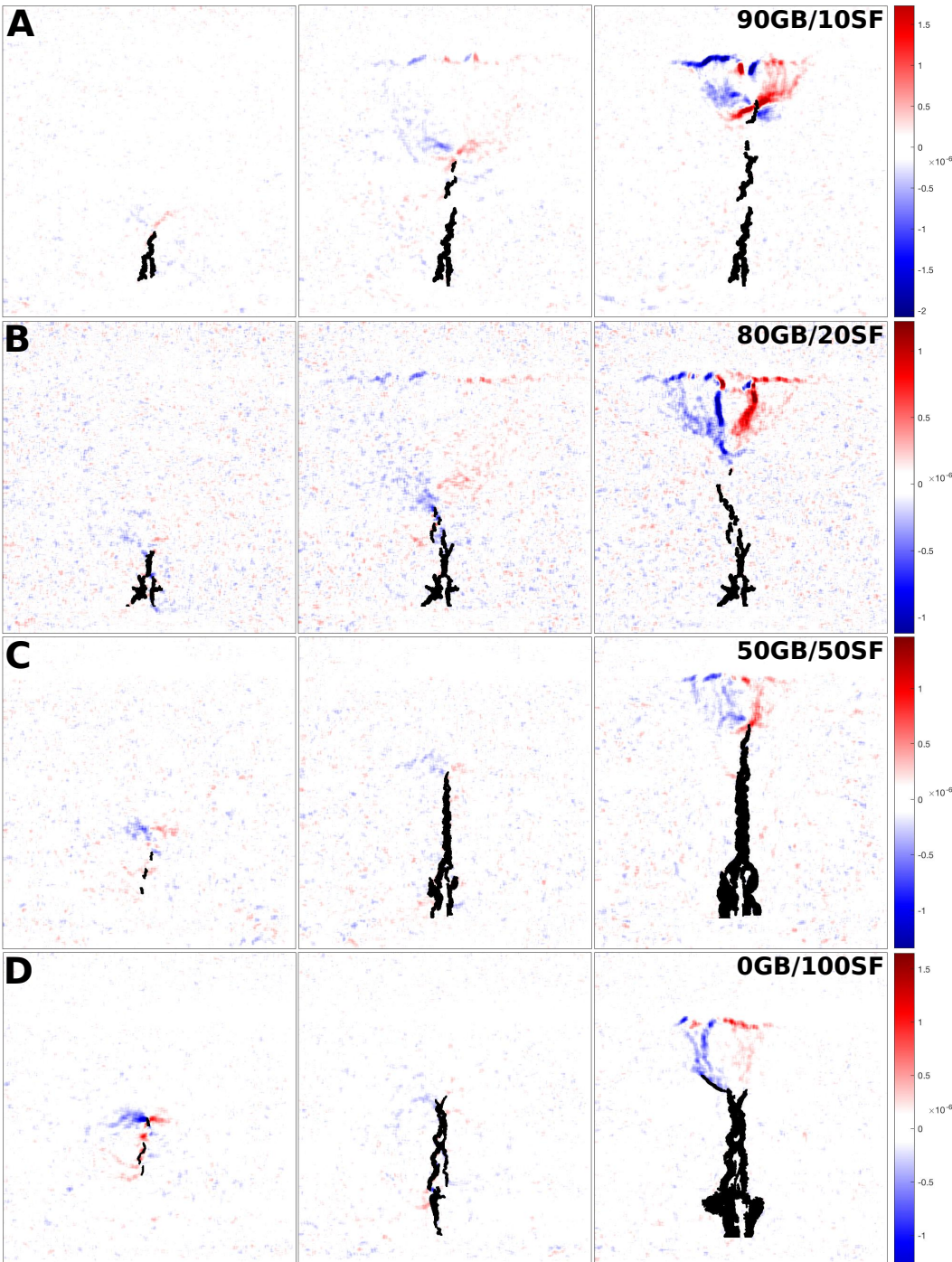


Figure 8.

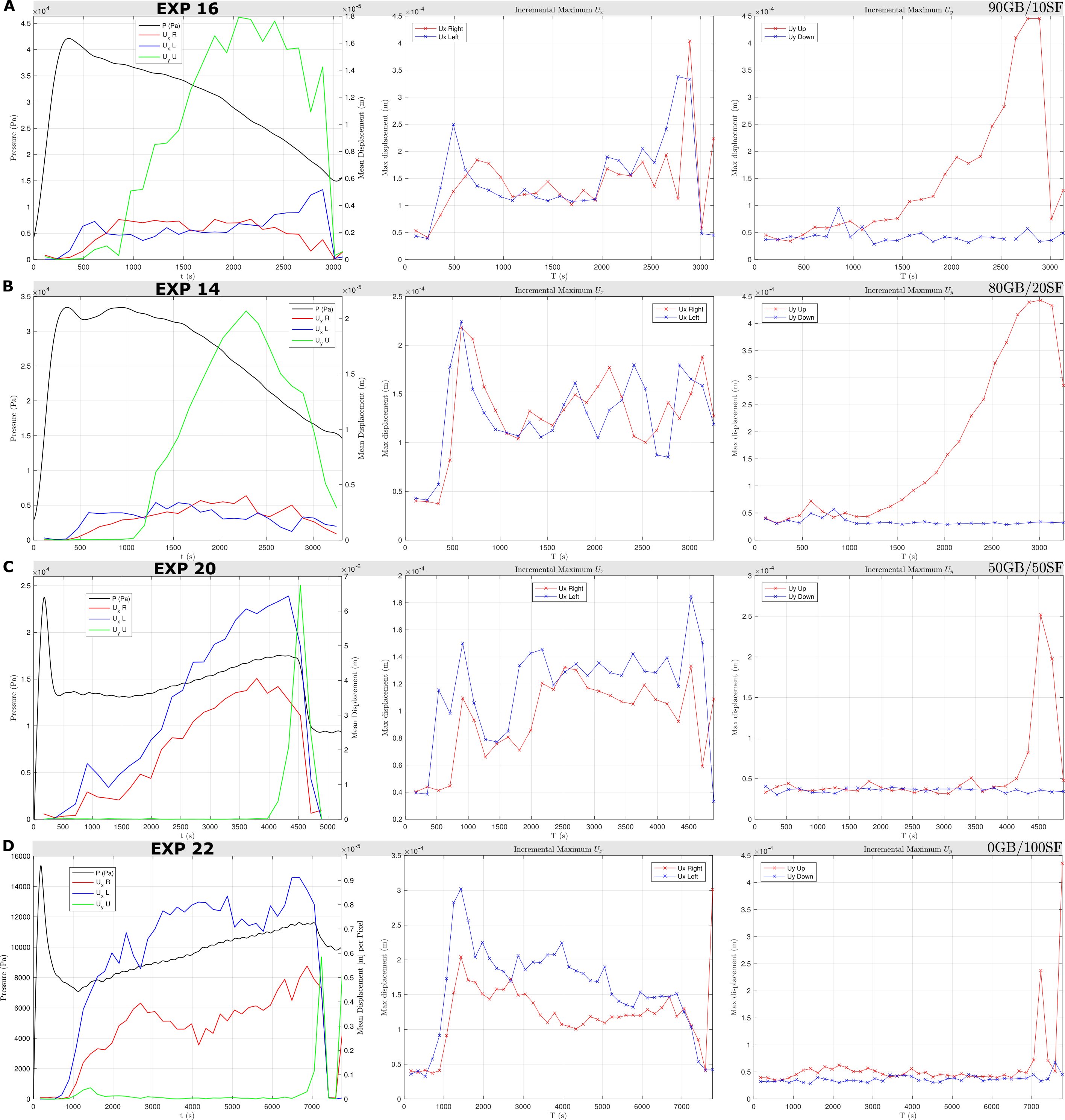
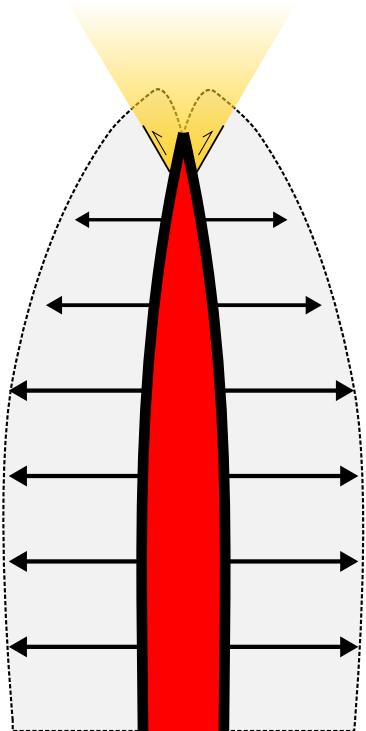
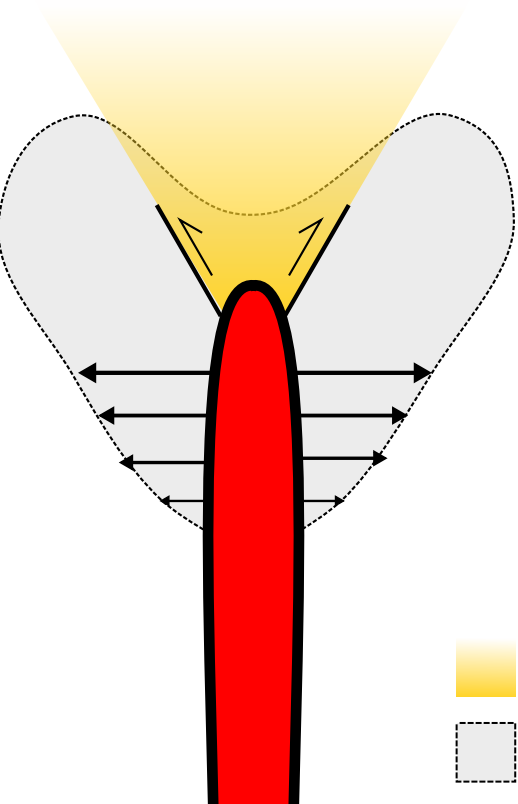


Figure 9.

High Cohesion Host



Low Cohesion Host



-  Vertical Uplift
-  Horizontal Opening